



# 1 The Canadian Earth System Model version 5 (CanESM5.0.3)

2 Neil C. Swart<sup>1,3</sup>, Jason N.S. Cole<sup>1</sup>, Viatcheslav V. Kharin<sup>1</sup>, Mike Lazare<sup>1</sup>, John F. Scinocca<sup>1</sup>, Nathan P.  
3 Gillett<sup>1</sup>, James Anstey<sup>1</sup>, Vivek Arora<sup>1</sup>, James R. Christian<sup>1,2</sup>, Sarah Hanna<sup>1</sup>, Yanjun Jiao<sup>1</sup>, Warren G. Lee<sup>1</sup>,  
4 Fouad Majaess<sup>1</sup>, Oleg A. Saenko<sup>1</sup>, Christian Seiler<sup>4</sup>, Clint Seinen<sup>1</sup>, Andrew Shao<sup>3</sup>, Larry Solheim<sup>1</sup>, Knut  
5 von Salzen<sup>1,3</sup>, Duo Yang<sup>1</sup>, Barbara Winter<sup>1</sup>

6

7 <sup>1</sup>Canadian Centre for Climate Modelling and Analysis, Environment and Climate Change Canada, Victoria, BC, V8W 2P2,  
8 Canada

9 <sup>2</sup>Fisheries and Oceans Canada, Institute of Ocean Sciences, Sidney, BC, Canada.

10 <sup>3</sup>University of Victoria, 3800 Finnerty Rd, Victoria, BC, V8P 5C2, Canada.

11 <sup>4</sup>Climate Processes Section, Environment and Climate Change Canada, Victoria, BC, V8P 5C2, Canada.

12 *Correspondence to:* Neil C. Swart (neil.swart@canada.ca)

13 **Abstract.** The Canadian Earth System Model version 5 (CanESM5) is a global model developed to simulate historical climate  
14 change and variability, to make centennial scale projections of future climate, and to produce initialized seasonal and decadal  
15 predictions. This paper describes the model components and their coupling, as well as various aspects of model development,  
16 including tuning, optimization and a reproducibility strategy. We also document the stability of the model using a long control  
17 simulation, quantify the model's ability to reproduce large scale features of the historical climate, and evaluate the response of  
18 the model to external forcing. CanESM5 is comprised of three dimensional atmosphere (T63 spectral resolution / 2.8°) and  
19 ocean (nominally 1°) general circulation models, a sea ice model, a land surface scheme, and explicit land and ocean carbon  
20 cycle models. The model features relatively coarse resolution and high throughput, which facilitates the production of large  
21 ensembles. CanESM5 has a notably higher equilibrium climate sensitivity (5.7 K) than its predecessor CanESM2 (3.8 K),  
22 which we briefly discuss, along with simulated changes over the historical period. CanESM5 simulations are contributing to  
23 the Coupled Model Intercomparison Project Phase 6 (CMIP6), and will be employed for climate science and service  
24 applications in Canada.

25

26

27

28



## 29 **1 Introduction**

30 A multitude of evidence shows that human influence is driving accelerating changes in the climate system, which are  
31 unprecedented in millennia (IPCC, 2013). As the impacts of climate change are increasingly being felt, so is the urgency to  
32 take action based on reliable scientific information (UNFCCC, 2015). To this end, the Canadian Centre for Climate Modelling  
33 and Analysis (CCCma) is engaged in an ongoing effort to improve modelling of the global earth system, with the aim of  
34 enhancing our understanding of climate system function, variability and historical changes, and for making improved  
35 quantitative predictions and projections of future climate. The global coupled model, CanESM, forms the basis of the CCCma  
36 modelling system, which also includes the Canadian Regional Climate Model (CanRCM) for finer scale modelling of the  
37 atmosphere (Scinocca et al., 2016), the Canadian Middle Atmosphere Model (CMAM) with atmospheric chemistry (Scinocca  
38 et al., 2008), and the Canadian Seasonal to Interseasonal Prediction System which is used for seasonal prediction and decadal  
39 forecasts (CanSIPS, Merryfield et al., 2013).

40  
41 CanESM5 is the current version of CCCma's global model, and has a pedigree extending back 40 years to the introduction of  
42 the first atmospheric General Circulation Model (GCM) developed at CCCma's predecessor, the Canadian Climate Centre  
43 (Boer and McFarlane, 1979; Boer et al., 1984; McFarlane, et al., 1992). Successive versions of the model introduced a dynamic  
44 three dimensional ocean in CGCM1 (Flato et al., 2000; Boer et al. 2000a; Boer et al. 2000b), and later an interactive carbon  
45 cycle was included to form CanESM1 (Arora et al, 2009; Christian et al., 2010). The last major iteration of the model,  
46 CanESM2 (Arora et al, 2011), was used in the Coupled Model Intercomparison Project phase 5 (CMIP5), and continues to be  
47 employed for novel science applications such as generating large initial condition ensembles for detection and attribution (e.g.  
48 Kirchmeier-Young et al., 2017; Swart et al., 2018).

49  
50 As detailed below, CanESM5 represents a major update to CanESM2. The update includes incremental improvements to the  
51 atmosphere, land surface and terrestrial ecosystem models. The major changes relative to CanESM2 are the implementation  
52 of completely new models for the ocean, sea-ice, marine ecosystems, and a new coupler. Model developers have a choice in  
53 distributing increasing, but finite, computational resources between improvements in model resolution, model complexity and  
54 model throughput (i.e. number of years simulated). The resolution of CanESM5 (T63 or  $\sim 2.8^\circ$  in the atmosphere and  $\sim 1^\circ$  in  
55 the ocean) remains similar to CanESM2, and is at the lower end of the spectrum of CMIP6 models. The advantage of this  
56 coarse resolution is a relatively high model throughput given the complexity of the model, which enables many years of  
57 simulation to be achieved with available computational resources. The first major application of CanESM5 is CMIP6 (Eyring  
58 et al., 2016), and over 50,000 years of simulation are being conducted for the 20 CMIP6-endorsed MIPs in which CCCma is  
59 participating.

60

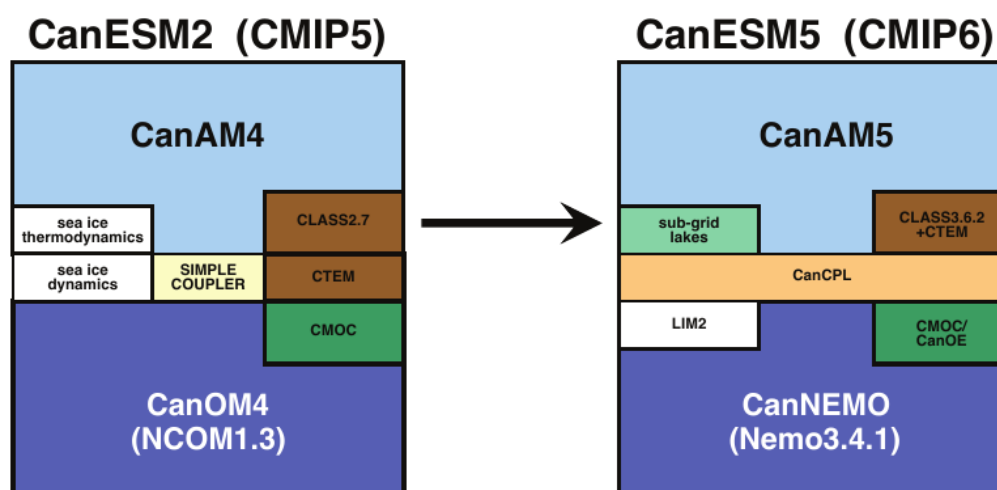


61 The aim of this paper is to provide a comprehensive reference that documents CanESM5. In the sections below, each of the  
62 model components is briefly described, and we also explain the approach used to develop, tune and numerically optimize the  
63 model. Following that, we document the stability of the model in a long pre-industrial control simulation, and the model's  
64 ability to reproduce large-scale features of the climate system. Finally, we investigate the sensitivity of the model to external  
65 forcings.

## 66 2 Component Models

67 In CanESM5 the atmosphere is represented by the Canadian Atmosphere Model (CanAM5), which incorporates the Canadian  
68 Land Surface Scheme (CLASS) and the Canadian Terrestrial Ecosystem Model (CTEM). The ocean is represented by a  
69 CCCma customized version of the Nucleus for European Modelling of the Ocean model (NEMO), with ocean biogeochemistry  
70 represented by either the Canadian Model of Ocean Carbon (CMOC) in the standard model version labelled as *CanESM5*, or  
71 the Canadian Ocean Ecosystem model (CanOE) in versions labelled *CanESM5-CanOE*. The atmosphere and ocean  
72 components are coupled by means of the Canadian Coupler (CanCPL). These components of CanESM5 are summarized  
73 schematically in Fig. 1, and described further below.

74



75

76 **Figure 1: Model schematic, showing the evolution of components between CanESM2 and CanESM5.**

77

### 78 2.1 The Canadian Atmospheric Model version 5 (CanAM5)

79 Version 5 of the Canadian Atmospheric Model (CanAM5) has several improvements relative to its predecessor, CanAM4 (von  
80 Salzen et al., 2013), including changes to aerosol, clouds, radiation, land surface and lake processes. The model uses a T63



81 triangular spectral truncation in the model dynamical core, with an approximate horizontal resolution of 2.8 degrees in  
82 latitude/longitude. It uses a hybrid vertical coordinate system with 49 levels between the surface and 1 hPa, with a vertical  
83 resolution of about 100 m near the surface. Relative to the 35 levels used in CanESM2 most of the additional 14 levels were  
84 added in the upper troposphere and stratosphere. The representation of radiative processes was improved through changes to  
85 the parameterization of albedos for bare soil, snow and ocean white-caps; cloud optics for ice clouds and polluted liquid clouds;  
86 improved aerosol optical properties; and absorption by the water vapour continuum at solar wavelengths. For aerosols, the  
87 emission of mineral dust and dimethyl sulfide (DMS) was improved while for clouds a parameterization of the second indirect  
88 effect was activated in the stratiform cloud microphysics.

89  
90 Parameterizations of surface processes were improved through an upgrade of the land surface scheme from CLASS 2.7 to  
91 3.6.2 as well as the inclusion of a parameterization for sub-grid lakes. CanESM5 represents the first coupled model produced  
92 by the CCCma in which the atmosphere and ocean do not employ coincident horizontal computational grids. As a  
93 consequence, CanAM5 was modified to support a fractional land mask, by generalizing its underlying surface to support grid-  
94 box fractional tiles of land and water. This tiling technology was extended to include land surface components of ocean, sea-  
95 ice and subgrid scale lakes. In this way appropriate fluxes are provided to each model component. A more detailed description  
96 of CanAM5 will be provided in a companion paper in this special issue (Cole et al., 2019).

## 97 **2.2 CLASS-CTEM**

98 The CLASS-CTEM modelling framework consists of the Canadian Land Surface Scheme (CLASS) and the Canadian  
99 Terrestrial Ecosystem Model (CTEM) which together form the land component of CanESM5. CLASS and CTEM simulate  
100 the physical and biogeochemical land surface processes, respectively, and together they calculate fluxes of energy, water, CO<sub>2</sub>  
101 and wetland CH<sub>4</sub> emissions at the land-atmosphere boundary. The introduction of dynamic wetlands and their methane  
102 emissions is a new biogeochemical process added since the CanESM2.

103  
104 CLASS is described in detail in Verseghy (1991), Verseghy et al. (1993) and Verseghy (2000) and version 3.6.2 is used in  
105 CanESM5. It prognostically calculates the temperature for its soil layers, their liquid and frozen moisture contents, temperature  
106 of a single vegetation canopy layer if it is present as dictated by the specified land cover, and the snow water equivalent and  
107 temperature of a single snow layer if it is present. Three permeable soil layers are used with default thicknesses of 0.1, 0.25  
108 and 3.75 m. The depth to bedrock is specified on the basis of the global data set of Zabler (1986) which reduces the thicknesses  
109 of the permeable soil layers. CLASS performs energy and water balance calculations and all physical land surface processes  
110 for four plant functional types (PFTs) (needleleaf trees, broadleaf trees, crops and grasses), and operates at the same sub-daily  
111 time step as the rest of the atmospheric component.

112



113 CTEM models photosynthesis, autotrophic respiration from its three living vegetation components (leaves, stem and roots)  
114 and heterotrophic respiration fluxes from its two dead carbon components (litter and soil carbon) and is described in detail in  
115 Arora (2003), Arora and Boer (2003) and Arora and Boer (2005). Land use change is also modelled on the basis of specified  
116 time-varying land cover which incorporates the increase in crop area over the historical period following Arora and Boer  
117 (2010). CTEM's photosynthesis module operates within CLASS, at the same time step as rest of the atmospheric component.  
118 CTEM provides CLASS with dynamically simulated structural attributes of vegetation including leaf area index (LAI),  
119 vegetation height, rooting depth and distribution, and above ground canopy mass. All terrestrial ecosystem processes other  
120 than photosynthesis are modelled in CTEM at a daily time step. Terrestrial ecosystem processes in CTEM are modelled for  
121 nine PFTs that map directly to the PFTs used by CLASS. Needleleaf trees are divided into their deciduous and evergreen types,  
122 broadleaf trees are divided into cold and drought deciduous and evergreen types, and crops and grasses are divided into C<sub>3</sub> and  
123 C<sub>4</sub> versions based on their photosynthetic pathways.

124

125 The calculation of wetland extent and methane emissions from wetlands is described in detail in Arora et al. (2018). In brief,  
126 dynamic wetland extent is based on the “flat” fraction in each grid cell with slopes less than 0.2%. As the liquid soil moisture  
127 in the top soil layer increases above a specified threshold, the wetland fraction increases linearly up to a maximum value, equal  
128 to the flat fraction in a grid cell. The simulated CH<sub>4</sub> emissions from wetlands are calculated by scaling the heterotrophic  
129 respiration flux from the model's litter and soil carbon pools to account for the ratio of wetland to upland heterotrophic  
130 respiratory flux and the fact that some of the CH<sub>4</sub> flux is oxidized in the soil column before reaching the atmosphere.

131

132 Specified land cover that includes fractional coverages of CTEM's nine PFTs is generated based on a potential vegetation  
133 cover for 1850 upon which the 1850 crop cover is superimposed. From 1850 onwards, as the fractional area of C<sub>3</sub> and C<sub>4</sub> crops  
134 changes the fractional coverages of the other non-crop PFTs are adjusted linearly in proportion to their existing coverage, as  
135 described in Arora and Boer (2010). The increase in crop area over the historical period is based on LUH2 v2h product  
136 (<http://luh.umd.edu/data.shtml>) of the land use harmonization (LUH) effort (Hurtt et al., 2011).

137

138 Surface runoff and baseflow simulated by CLASS are routed through river networks. Major river basins are discretized at the  
139 resolution of the model and river routing is performed at the model resolution using the variable velocity river routing scheme  
140 presented in Arora and Boer (1999). The delay in routing is caused by the time taken by runoff to travel over land in an assumed  
141 rectangular river channel and a ground water component to which baseflow contributes. Streamflow (i.e. the routed runoff)  
142 contributes fresh water to the ocean grid cell where the land fraction of a CanAM grid cell first drops below 0.5 along the river  
143 network as the river approaches the ocean.

144

145 In CanESM5, glacier coverage is specified and static. Grid cells are specified as glacier if the fraction of the grid cell covered  
146 by ice exceeds 40%, based on the GLC2000 dataset (Bartholomé and Belward, 2005). The combination of this threshold and



147 the model resolution results in glacier covered cells predominantly representing the Antarctic and Greenland ice sheets, with  
148 a few glacier cells in the Himalayas, Northern Canada and Alaska. Snow can accumulate on glaciers, and any additional snow  
149 above the threshold of  $100 \text{ kg m}^{-2}$  of snow water equivalent is “converted into ice”, and an equivalent mass of freshwater is  
150 immediately inserted into runoff – implicitly representing mass balance between accumulation and calving. Snow and ice on  
151 glaciers can be melted, with the water exceeding a ponding limit inserted into runoff. There is no explicit accounting for glacier  
152 mass balance, or adjustment of glacier coverage. This represents a potentially infinite global source or sink of fresh water in  
153 the coupled system, particularly in climates which are far from the state represented by GLC2000. However, in practice the  
154 timescales of our centennial-scale simulations are much shorter than the response times of ice sheet coverage, and any  
155 imbalances are small (Section 4).

### 156 **2.3 NEMO modified for CanESM (CanNEMO)**

157 The ocean component is based on NEMO version 3.4.1 (Madec et al. 2012). It is configured on the tripolar ORCA1 C-grid  
158 with 45 z-coordinate vertical levels, varying in thickness from  $\sim 6 \text{ m}$  near the surface to  $\sim 250 \text{ m}$  in the abyssal ocean.  
159 Bathymetry is represented with partial cells. The horizontal resolution is based on a  $1^\circ$  Mercator grid, varying with the cosine  
160 of latitude, with a refinement of the meridional grid spacing to  $1/3^\circ$  near the Equator. The adopted model settings include the  
161 linear free surface formulation (see Madec et al. 2012 and references therein). Momentum and tracers are mixed vertically  
162 using a turbulent kinetic energy scheme based on the model of Gaspar et al. (1990). The tidally-driven mixing in the abyssal  
163 ocean is accounted for following Simmons et al. (2004). Base values of vertical diffusivity and viscosity are  $0.5 \times 10^{-5}$  and  
164  $1.5 \times 10^{-4} \text{ m}^2/\text{s}$ , respectively. A parameterization of double diffusive mixing (Merryfield et al., 1999) is also included. Lateral  
165 viscosity is parameterized by a horizontal Laplacian operator with eddy viscosity coefficient of  $1.0 \times 10^4 \text{ m}^2/\text{s}$  in the tropics,  
166 decreasing with latitude as the grid spacing decreases. Tracers are advected using the total variance dissipation scheme  
167 (Zalesak, 1979). Lateral mixing of tracers (Redi 1982) is parameterized by an isoneutral Laplacian operator with eddy  
168 diffusivity coefficient of  $1. \times 10^3 \text{ m}^2/\text{s}$  at the Equator, which decreases poleward with the cosine of latitude. The process of  
169 potential energy extraction by baroclinic instability is represented with the Gent and McWilliams (1990) scheme using a  
170 spatially-variable formulation for the mesoscale eddy transfer coefficient, as briefly described below.

171  
172 Two modifications have been introduced to the NEMO's mesoscale and small-scale mixing physics. The first modification is  
173 motivated by the observational evidence suggesting that away from the tropics the eddy scale decreases less rapidly than does  
174 the Rossby radius (e.g., Chelton et al., 2011). This is taken into consideration in the formulation for the eddy mixing length  
175 scale, which is used to compute the mesoscale eddy transfer coefficient for the Gent and McWilliams (1990) scheme (for  
176 details, see Saenko et al., 2018). The second modification is motivated by the observationally based estimates suggesting that  
177 a fraction of the mesoscale eddy energy could get scattered into high-wavenumber internal waves, the breaking of which results  
178 in enhanced diapycnal mixing (e.g., Marshall and Naveira Garabato, 2008; Sheen et al., 2014). A simple way to represent this



179 process in an ocean general circulation model was proposed in Saenko et al. (2012). Here, we employ an updated version of  
180 their scheme which accounts better for the eddy-induced diapycnal mixing observed in the deep Southern Ocean (e.g., Sheen  
181 et al., 2014).

182  
183 CanESM5 uses the LIM2 sea ice model (Fichefet and Morales Maqueda, 1997; Bouillon et al., 2009), which is run within the  
184 NEMO framework. Some details regarding the calculation of surface temperature over sea-ice are described in the coupling  
185 section below.

## 186 **2.4 Ocean biogeochemistry**

187 Two different ocean biogeochemical models, of differing complexity and expense, were developed in the NEMO framework:  
188 CMOC and CanOE. Two coupled models versions will be submitted to CMIP6. The version labelled as *CanESM5* uses CMOC  
189 and was used to run all the experiments that CCCma has committed to. The version labelled *CanESM5-CanOE*, described in  
190 another paper in this special issue (Christian et al., 2019), is identical to CanESM5, except that CMOC was replaced with  
191 CanOE, and this version has been used to run a subset of the CMIP6 experiments, including DECK and historical (see Section  
192 3.4). Both biogeochemical models simulate ocean carbon chemistry and abiotic chemical processes such as oxygen solubility  
193 identically, in accordance with the OMIP-BGC protocol (Orr et al., 2017).

### 194 **2.4.1 Canadian Model of Ocean Carbon (CMOC)**

195  
196 The Canadian Model of Ocean Carbon was developed for earlier versions of CanESM (Zahariev et al., 2008; Christian et al.,  
197 2010; Arora et al., 2011), and includes carbon chemistry and biology. The biological component is a simple Nutrient-  
198 Phytoplankton-Zooplankton-Detritus (NPZD) model, with fixed Redfield stoichiometry, and simple parameterizations of iron  
199 limitation, nitrogen fixation, and export flux of calcium carbonate. CMOC was migrated into the NEMO modelling system,  
200 and the following important modifications were made: i) oxygen was added as a passive tracer with no feedback on biology;  
201 ii) carbon chemistry routines were updated to conform to the OMIP-BGC protocol (Orr et al., 2017); iii) additional passive  
202 tracers requested by OMIP were added, including natural and abiotic DIC as well as the inert tracers CFC11, CFC12 and SF6.  
203

### 204 **2.4.2 Canadian Ocean Ecosystem Model (CanOE)**

205 The Canadian Ocean Ecosystem Model (CanOE) is a new ocean biology model with a greater degree of complexity than  
206 CMOC, and represents explicitly some processes that were highly parameterized in CMOC. CanOE has two size classes for  
207 each of phytoplankton, zooplankton and detritus, with variable elemental (C/N/Fe) ratios in phytoplankton and fixed ratios for  
208 zooplankton and detritus. Each detritus pool has its own distinct sinking rate. In addition, there is an explicit detrital CaCO<sub>3</sub>  
209 variable, with its own sinking rate. Iron is explicitly modelled, with a dissolved iron state variable, sources from aeolian



210 deposition and reducing sediments, and irreversible scavenging from the dissolved pool. N<sub>2</sub> fixation is parameterized similarly  
211 to CMOC with temperature- and irradiance-dependence and inhibition by Dissolved Inorganic Nitrogen, but no explicit N<sub>2</sub>-  
212 fixer group. In addition, N<sub>2</sub> fixation is iron-limited in CanOE. In CanOE, denitrification is modelled prognostically and occurs  
213 only where dissolved oxygen is <6 mmol m<sup>-3</sup>. Deposition of organic carbon is instantaneously remineralized at the sea floor  
214 as in CMOC, and CaCO<sub>3</sub> deposited at the sea floor dissolves if the calcite is undersaturated (whereas in CMOC the burial  
215 fraction is implicitly 100%). Carbon chemistry and all abiotic chemical processes such as oxygen solubility conform to the  
216 OMIP-BGC protocol (Orr et al., 2017) and are identical in CanOE and CMOC, except that in CMOC the carbon chemistry  
217 solver is applied only in the surface layer (as there is no feedback from saturation state to other biogeochemical processes in  
218 the subsurface layers). CanOE has roughly twice the computational expense of CMOC.

## 219 **2.5 The Canadian Coupler (CanCPL)**

220 CanCPL is a new coupler developed to facilitate communication between CanAM and CanNEMO. CanCPL depends on Earth  
221 System Modeling Framework (ESMF) library routines for regridding, time advancement, and other miscellaneous  
222 infrastructure (Theurich et al., 2016; Collins et al., 2005; Hill et al., 2004). It was designed for the Multiple Program Multiple  
223 Data (MPMD) execution mode, with communication between the model components and the coupler via the Message Passing  
224 Interface (MPI).

225  
226 The fields passed between the model components are summarized in Tables A1 to A4. In general, CanNEMO passes  
227 instantaneous prognostic fields, which are remapped by CanCPL and given to CanAM as lower boundary conditions. These  
228 prognostic fields (sea surface temperature, sea-ice concentration and mass of sea-ice and snow) are held constant in CanAM  
229 over the course of the coupling cycle. After integrating forward for a coupling cycle, CanAM passes back fluxes, averaged  
230 over the coupling interval, which are remapped in CanCPL and passed on to NEMO as surface boundary conditions. An  
231 exception is the ocean surface CO<sub>2</sub> flux, which is computed in CanNEMO and passed to CanAM. CanAM and CanNEMO are  
232 run in parallel, and the timing of exchanges through the coupler is indicated schematically in Fig. 2.

233  
234 All regridding in CanCPL is done using the ESMF first order conservative regridding option (ESMF, 2018), ensuring that  
235 global integrals remain constant for all quantities passed between component models (but see an exception below). The  
236 remapping weights  $w_{ij}$ , for a particular source cell  $i$  and destination cell  $j$  are given by:  $w_{ij} = f_{ij} \times A_{si} / (A_{dj} \times D_j)$ , where  
237  $f_{ij}$  is the fraction of the source cell  $i$  contributing to the destination cell  $j$ ,  $A_{si}$  and  $A_{dj}$  are the areas of the source and destination  
238 cells, and  $D_j$  is the fraction of the destination cell that intersects the unmasked source grid (ESMF, 2018).

239  
240



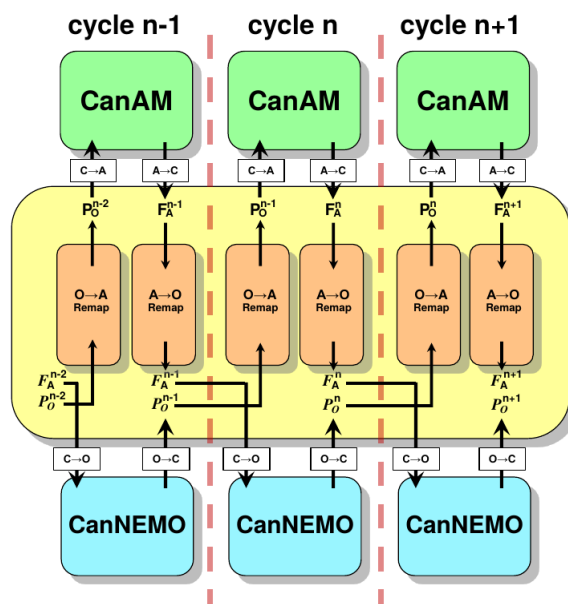


**Figure 2: Schematic showing the ordering of exchanges between CanCPL and CanAM and CanNEMO. Prognostic fields ( $P_O$ ) are passed from NEMO to the coupler, remapped, and passed to CanAM. Fluxes ( $F_A$ ) are passed from CanAM, remapped in CanCPL, and passed NEMO to complete the next coupling cycle. Superscripts denote the coupling cycle, e.g. Prognostic fields from NEMO are passed to CanCPL at the end of cycle “n”, remapped, and used in CanAM during cycle “n+1”.**

Within the NEMO coupling interface the “conservative” coupling option is employed. This option dictates that net fluxes are passed over the combined ocean-ice cell, and the fluxes over only the ice covered fraction of the cell are also supplied, in principle allowing net conservation, even if the distribution of ice has changed given the unavoidable one coupling cycle lag encountered in parallel coupling mode. It was verified that the net heat fluxes passed from CanAM were identical to the net fluxes received by NEMO, to the level of machine precision. Conservation in the coupled model piControl run is discussed further in Section 4.

Sea-ice thermodynamics are computed in the LIM2 ice model, based on the surface fluxes received from CanAM, and the basal heat flux from the NEMO liquid ocean. LIM2 provides the sea-ice concentration, snow and ice thickness to CanAM, via the coupler. The surface flux calculation in CanAM5 requires the ground temperature at the snow/sea-ice interface,  $GT_{ice}$ . The  $GT_{ice}$  for this purpose can be passed from LIM2 to CanAM once each coupling cycle, or an alternative  $GT_{ice}$  can be evaluated in CanAM at every model time step, taking into account evolving surface albedo and atmospheric temperature (e.g. West et al., 2016). As implemented, when computing  $GT_{ice}$ , CanAM independently computes the conductive heat flux through sea-ice, and there is no constraint that this flux, or  $GT_{ice}$  is the same as that in LIM2. Conservation is maintained because the net



262 heat flux between the atmosphere and sea-ice is computed in CanAM and applied to LIM2, but different ice surface  
263 temperatures could result. Both approaches to computing surface fluxes were tested in CanESM5 and no major impacts on sea-  
264 ice or the broader climate system relative to the default model were discovered. However, a significantly shorter coupling  
265 cycle of one hour was required for convergence when fluxes were computed from the LIM2  $GT_{ice}$  passed through the coupler.  
266 The shorter coupling period was required to more physically resolve the response to diurnal variations in radiative and sensible  
267 heat fluxes from the atmosphere (see for example West et al., 2016). The evaluation of fluxes from  $GT_{ice}$  computed in CanAM,  
268 on the other hand, was stable for coupling periods ranging from 1 to 24 hours with no major changes in the mean climate, or  
269 variability immediately apparent. A final coupling cycle interval of three hours was implemented for CanESM5 with the  
270 computation of fluxes based on the CanAM evaluation of  $GT_{ice}$ . These choices represented improved robustness and a  
271 compromise between greater efficiency (i.e. longer coupling periods) and maximum “realism”, which would be the one hour  
272 coupling dictated by the length of the NEMO time step.

273

274 After a significant number of CMIP6 production simulations were complete, it was determined that while conservative  
275 remapping was desirable for heat and water fluxes, it introduced issues in the wind-stress field passed from CanAM to  
276 CanNEMO. Specifically, since CanAM is nominally three times coarser than CanNEMO, conservative remapping resulted in  
277 constant wind-stress fields over several NEMO grid-cells, followed by an abrupt change at the edge of the next CanAM cell.  
278 This blockiness in the wind-stress results in a non-smooth first derivative, and the resulting peaked wind-stress curl results in  
279 unphysical features in, for example, the ocean vertical velocities. Changing regridding of only wind-stresses to the more typical  
280 “bilinear” interpolation, instead of “conservative” remapping, largely alleviates this issue. Sensitivity tests indicate no major  
281 impact on gross climate change characteristics such as transient climate response or equilibrium climate sensitivity, or on  
282 general features of the surface climate. However there is an impact on local ocean dynamics, which led to the decision to  
283 submit a “perturbed” physics member to CMIP6. Hence, simulations submitted to CMIP6 labelled as perturbed physics  
284 member 1 (“p1”) use conservative remapping for wind stress, while those labelled as “p2” use bilinear regridding (see Section  
285 3.4). A comparison between p1 and p2 runs is provided in Appendix E.

## 286 **3 Model development and deployment**

### 287 **3.1 Model tuning and spin up**

288 Each of the CanESM5 component models, CanAM5, CLASS-CTEM and CanNEMO, were initially developed independently  
289 under driving by observations in stand-alone configurations - CanAM5 in present-day (2003-2008) AMIP mode and  
290 CanNEMO in preindustrial (PI) OMIP-like mode using CORE bulk formulae. In these configurations, free parameters were  
291 initially adjusted to reduce climatological biases assessed via a range of diagnostics. Further details of the CanAM5 tuning  
292 may be found in Cole et al. (2019). The component models were then brought together in a preindustrial configuration (i.e.  
293 the piControl experiment), which was evaluated based on an array of diagnostics. Several thousand years of coupled simulation



294 was run during the finalization of model, and an approach was taken whereby AMIP simulations would be used to derive  
295 parameter adjustments in CanAM, which would then be applied to the coupled model.

296

297 Initial present-day configurations of CanAM5 that were tuned to give roughly the observed top of the atmosphere net radiative  
298 forcing (TOA forcing  $\sim 0.7\text{--}1.0\text{ W m}^{-2}$ ) in an AMIP simulation produced coupled piControl simulations that were too cold  
299 (global mean near-surface temperatures below  $12^\circ\text{C}$ ), with extensive sea-ice and a collapsing meridional overturning  
300 circulation. One contributor to the tendency of the new coupled model to cool was the inclusion of the thermodynamic  
301 consequences of snow melt in the open ocean, which induces an average global cooling of  $\sim 0.5\text{ W m}^{-2}$  in the piControl, and  
302 was not included in the previous version, CanESM2.

303

304 This initial coupled-model cold bias was rectified by adjusting free parameters in CanAM, CLASS and LIM2, in order to  
305 achieve a piControl simulation with a global mean screen temperature of around  $13.7^\circ\text{C}$  (roughly the absolute value provided  
306 for 1850-1900 by the NASA-GISS, Berkeley Earth and HadCRUT4 datasets), and a sea-ice volume within the spread of  
307 CMIP5 models. The specific parameters adjusted were: emissivity of snow (from 1 to 0.97), snow grain size on sea-ice, the  
308 drainage parameter controlling soil moisture, the LIM2 parameter controlling the lead closure rate (from 2.0 to 3.0), and most  
309 significantly the accretion rate in cloud microphysics. The accretion rate exerted the largest control, and sensitivity to this  
310 parameter is described more fully in a companion paper (Cole et al., 2019).

311

312 The consequence of the adjustments in CanAM5 was an increase in the present day TOA forcing in AMIP mode from  $\sim 1$   
313  $\text{W/m}^2$  to  $\sim 2.5\text{ W m}^{-2}$ . Nonetheless, historical simulations of the coupled CanESM5 initialized from its equilibrated piControl  
314 show an increase in TOA forcing roughly matching the observed values of  $\sim 0.7\text{--}1.0\text{ W m}^{-2}$  over the 2003-2008 period for  
315 which CanAM5 was tuned in AMIP mode. The difference in patterns of SST and sea-ice concentrations between the coupled  
316 model and observations are thought to be the cause of these differences in TOA balance between coupled and AMIP mode.

317

318 The final adjustment was to the carbon uptake over land so as to better match the observed value over the historical period,  
319 and achieved via the parameter which controls the strength of the  $\text{CO}_2$  fertilization effect (Arora and Scinocca, 2016). No more  
320 extensive tuning of CanESM5 was undertaken. Critically, no tuning was undertaken on the climate system response to forcing  
321 - the transient and equilibrium climate sensitivity of CanESM5 are purely emergent properties. Once the tuned final  
322 configuration of CanESM5 was available, ocean potential temperature and salinity fields were initialized from World Ocean  
323 Atlas 2009, while CanAM, CLASS-CTEM and CMOC were initialized from the restarts from earlier development runs. The  
324 model was spun up for over 1500 years prior to the launch of the official CMIP6 piControl simulation, which extends for a  
325 further 2000 years.

326



### 327 3.2 Code management, version control and reproducibility

328 CanESM5 is the first version of the model to be publicly released, and this code sharing has been facilitated by the adoption  
329 of a new version control based strategy for code management. Additional goals of this new system are to adopt industry  
330 standard software development practises, to improve development efficiency, and to make all CanESM5 CMIP6 simulations  
331 fully repeatable.

332  
333 To maintain modularity, the code is organized such that each model component has a dedicated *git* repository for the version  
334 control of its source code (Table 1). A dedicated *super repository* tracks each of the components as *git submodules*. In this  
335 way, the *super repo.* keeps track of which specific versions of each component combine together to form a functional version  
336 of CanESM. A commit of the CanESM super repo., which is representable by an 8 character truncated SHA1 checksum, hence  
337 uniquely defines a version of the full CanESM source code. The model development process follows an industry standard  
338 workflow (Table B1). New model features are merged onto the *develop\_canesm* branch, which reflects the ongoing  
339 development of the model. Specific model versions, such as that used for CMIP6, are given tags and issued DOIs for ease of  
340 reference. We use an internal deployment of *gitlab* to host the model code and associated issue trackers, and we mirror the  
341 code to the public, online code hosting platform at [gitlab.com/ccma/canesm](https://gitlab.com/ccma/canesm).

342  
343 A dedicated ecosystem of software is used to configure, compile, run, and analyze CanESM simulations on ECCC's HPC  
344 (Table B2). Several measures are taken to ensure modularity and repeatability. The source code for each run is recursively  
345 cloned from gitlab and is fully self contained. A strict checking routine ensures that any code changes are committed to the  
346 version control system, and any run-specific configuration changes are captured in a dedicated configuration repository. A  
347 database records the SHA1 checksums of the particular model version and configuration used for every run, and these are  
348 included in CMIP6 NetCDF output for traceability. Input files for model initialization and forcing are also tracked for  
349 reproducibility (Table B1).

350  
351 Our strategy of version control, run isolation, strict checking and logging ensures that simulations can be repeated in the future,  
352 and the same climate will be obtained (bit identical reproducibility is a further step and is dependant on machine architecture  
353 and compilers). The implementation of a clear branching workflow, and the uptake of modern tools such as issue trackers, and  
354 the gitlab online code-hosting application has improved both collaboration and management of the code. This new system  
355 also led to large, unexpected improvements in model performance for two major reasons. The first was democratization of the  
356 code – via the promotion of group ownership of the code. The second was the freedom to experiment across the full code base  
357 ensured by our isolated run setup (Table B2), which was not possible under the previous system of using a single installed  
358 library of code shared across many runs. The performance gains achieved are described in the following section.

359



360 **Table 1: Code structure and repositories.**

Repository	Purpose
CanESM	The top-level super-repository, which tracks specific versions of the component <i>submodules</i> listed below, to form a function version of the model. Also contains a CONFIG directory with configuration files for the model.
CanAM	The source code for the spectral dynamics and physics of CanAM.
CanDIAG	Diagnostic source code for analyzing CanAM output, this repository also contains various scripting used to run the model.
CanNEMO	The CCCma modified NEMO source code, along with additional utility scripting.
CanCPL	The coupler source code.
CCCma_tools	A collection of software tools for compiling, running and diagnosing CanESM on ECCC's high performance computer.

361

### 362 **3.3 Model optimization and benchmarking**

363 The ECCC high performance computer system consists of the following components: a “backend” Cray XC40, with two 18  
364 core Broadwell CPUs per node (for 36 cores per node), and roughly 800 nodes in total, connected to a multi-PB lustre file  
365 system used as scratch space. This machine is networked to a “frontend” Cray CS5000, with several PB of attached HPFS  
366 spinning disk. This whole compute arrangement is replicated in a separate hall for redundancy, effectively doubling the  
367 available resources. Finally, a large tape-storage system (HPNLS) is available for archiving model results.

368

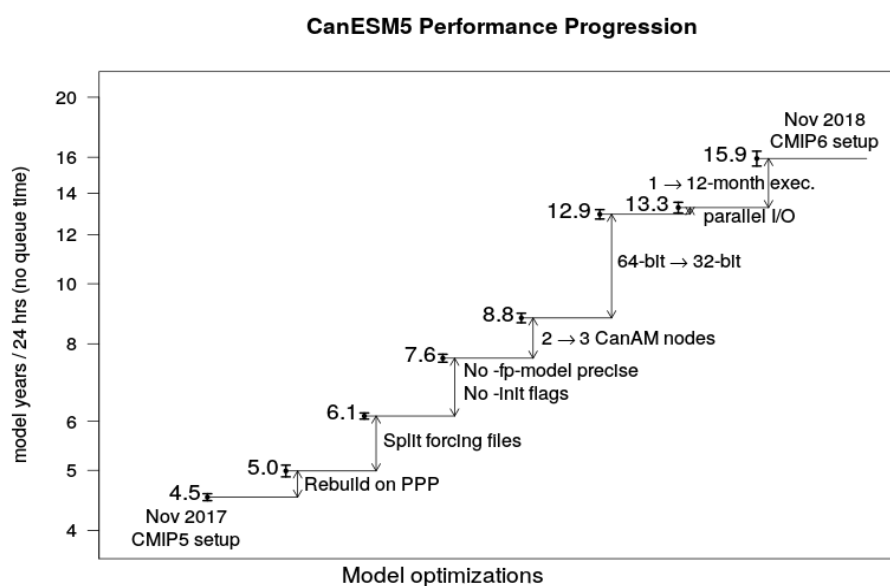
369 The initial implementation of a CanESM5 precursor on this new HPC occurred around Nov 1, 2017. The original workflow  
370 roughly followed that used for CanESM2 CMIP5 simulations. All CanESM5 components (atmosphere CanAM, coupler  
371 CanCPL and ocean CanNEMO) were originally running at 64-bit precision. The atmospheric component CanAM was running  
372 on two 36-core compute nodes, the coupler was running on a separate node, and the ocean component was running on 3 nodes,  
373 resulting in 6 nodes in total. The initial throughput on the system, without queue time, was around 4.6 years of simulation per  
374 wall-clock day (ypd), or alternatively 0.02 simulation years per core-day, when normalizing by the number of cores used.

375

376 In parallel to the physical model development, significant effort was made to improve the model throughput and eliminate a  
377 number of inefficiencies in the older CMIP5 workflow (Fig. 3). The largest effort was devoted to improving the efficiency of  
378 CanAM5, since this was identified as the major bottleneck. A brief summary of the improvements is given in Table C1 and  
379 Fig. 3. The most substantial and rewarding change was in converting the 64-bit CanAM component to 32-bit numerics. Since



380 the remaining two components, CanCPL and CanNEMO are still running at the 64-bit precision, the communication between  
381 CanAM and CanCPL required the promotion of a number of variables from 32-bit precision to 64-bit and back. The 32-bit  
382 CanAM implementation required a number of modifications to maintain the numerical stability of the code. Calculations in  
383 some subroutines, most notably in the radiation code, were promoted to the 64-bit accuracy. Conservation of some tracers, in  
384 particular CO<sub>2</sub>, was compromised at the 32-bit precision, and some additional code changes to conserve CO<sub>2</sub> and maintain  
385 carbon budgets were implemented. Significant effort was also invested in optimizing compiler options used for NEMO to  
386 maximize efficiency, while the scalability of the NEMO code allowed sensibly increasing the node count to keep pace with  
387 the accelerated 32-bit version of CanAM.



388  
389 **Figure 3: Schematic of CanESM5 optimization**

390  
391 In the final setup, the CanAM/CanCPL components are running on three shared compute nodes, and the ocean component  
392 CanNEMO is running on 5 nodes, resulting in 8 nodes overall. The combined effect of the improvements listed in Table C1  
393 resulted in more than tripling the original throughput to about 16 ypd (Fig. 3). Despite the increase in the total node count from  
394 6 to 8, the efficiency of the model also improved roughly three fold, from 0.02 simulation years per core day of compute to  
395 about 0.06 years per core day. This final model configuration can complete a realization of the 165 year CMIP6 historical  
396 experiment in just over 10 days, compared to about 36 days had no optimization been undertaken. At the time of writing, over  
397 50,000 years of CMIP6 related simulation had been conducted with CanESM5, consuming about one million core-days of  
398 compute time, resulting in about 8 PB of data archived to tape, and over 100 TB of data publicly served on the Earth System  
399 Grid Federation (ESGF).

400



### 3.4 Model experiments and scientific application

This section describes the major experiments and model variants of CanESM5 that are being conducted for the Coupled Model Intercomparison Phase 6 (CMIP6), the first major science application of the model. Fig. 4 shows the global mean surface temperature for several of the key CMIP6 experiments. Table 2 lists the variants of CanESM5 which are being submitted to CMIP6. These include the “p1” and “p2” perturbed physics members of CanESM5 (see Section 2.5), and a version of the model with a different ocean biogeochemistry model, CanESM5-CanOE.

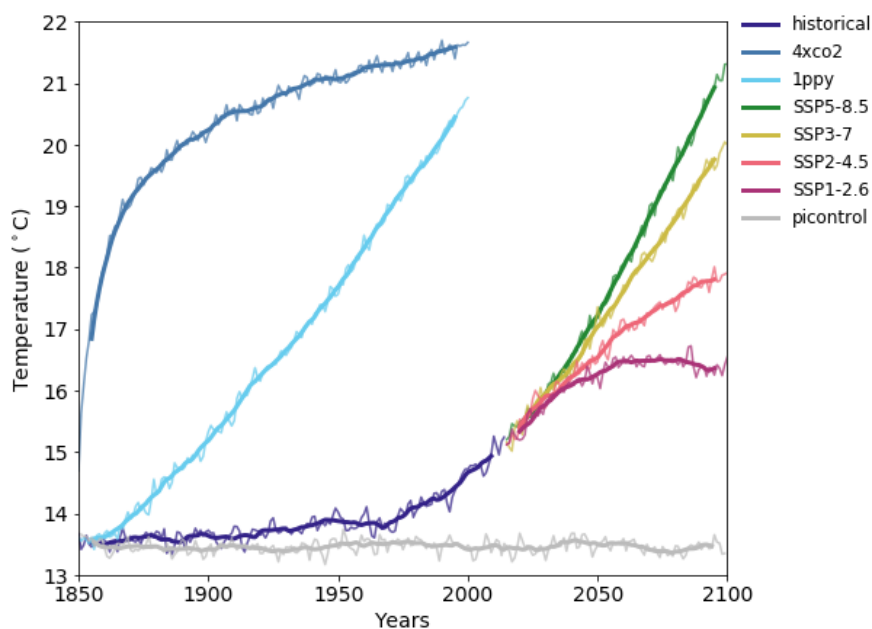


**Figure 4: Global average screen temperature in CanESM5 for the CMIP6 DECK experiments, as well as the historical and tier 1 SSP experiments (SSP5-85, SSP3-70, SSP2-45 and SSP1-26). Thick lines are the 11 year running means, thin lines are annual means.**

Table D1 lists the 20 CMIP6 endorsed MIPs in which CanESM5 is participating, and which model variants are being run for each MIP. The volume of simulation continues to grow, and will likely exceed 60,000 years. This is significantly more than the ~40,000 years of CMIP6 simulation estimated by Eyring et al. (2016). The major reason for this is that significantly larger ensembles have been produced than formally requested. For example, CanESM5 will submit at least 25 realizations for the historical and tier 1 SSP experiments, for each the “p1” and “p2” model variant, for a total of 50 realizations, significantly more than the single requested realization. The scientific value of such large initial condition ensembles has become evident (e.g. Kay et al., 2015; Kirchmeier-Young et al., 2017; Swart et al., 2018) and motivates this approach.



421 Individual historical realizations (ensemble members) of CanESM5 were generated by launching historical runs at 50 year  
422 intervals off the piControl simulation. This is the same as the approach used to generate the five realizations of CanESM2,  
423 which were submitted to CMIP5. The fifty year separation was chosen to allow for differences in multi-decadal ocean  
424 variability between realizations. Below we discuss the properties of the model, including illustrations of the internal variability  
425 generated spread across the historical ensemble. All results below are based on the CanESM5 p1 model variant.  
426

427 **Table 2: Model variants**

Model variant	Description
CanESM5 “p1”	CanESM5 realizations labelled as perturbed physics member 1 (“p1” in the variant label) have conservative remapping of wind-stress fields. The ocean biogeochemistry model is CMOC.
CanESM5 “p2”	CanESM5 realizations labelled as perturbed physics member 2 (“p2” in the variant label), use bilinear remapping of the wind-stress fields. A minor land-fraction change also occurs over Antarctica. The ocean biogeochemistry model is CMOC.
CanESM5-CanOE “p2”	CanESM5-CanOE is exactly the same physical model as CanESM5, but it uses the CanOE ocean biogeochemical model. All CanESM5-CanOE realizations use bilinear remapping of the wind-stress, and hence are labelled as perturbed physics member 2 (“p2” in the variant label). No “p1” variant is submitted. For physical climate purposes CanESM5 and CanESM5-CanOE may be treated as different realizations of the same model.

428

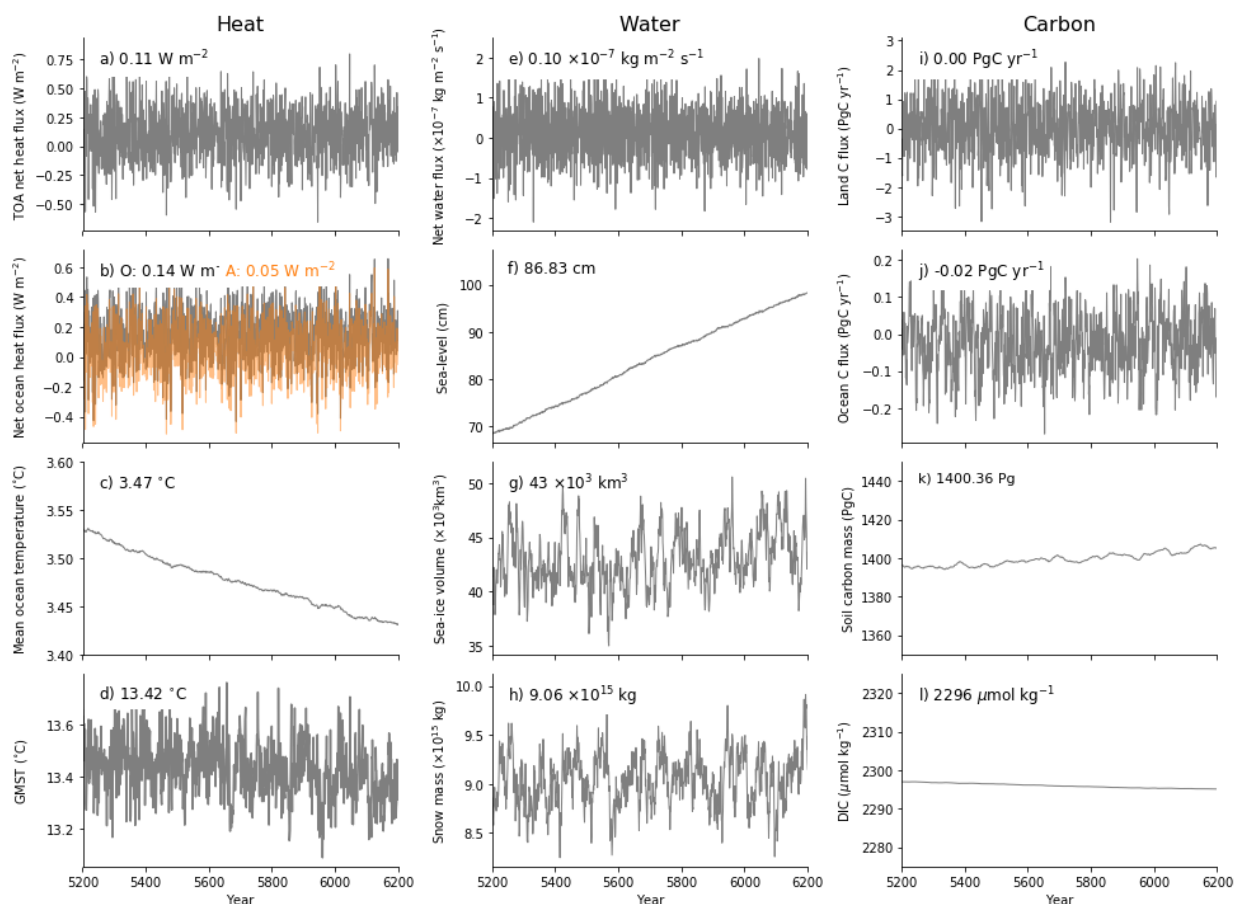
#### 429 **4 Stability of the pre-industrial control climate**

430 The characteristics and stability of the CanESM5 pre-industrial control climate are evaluated using 1000 years of simulation  
431 from the CMIP6 piControl experiment, conducted under constant specified greenhouse gas concentrations and forcings for the  
432 year 1850 (Eyring et al., 2016). Ideally, a climate model and all its subcomponents would exhibit perfect conservation of tracer  
433 mass (e.g. water, carbon), energy and momentum, and would be run for long enough to achieve equilibrium. In this case we  
434 would expect to see, on long term average, zero net fluxes of heat, freshwater and carbon at the interface between the  
435 atmosphere, ocean and land surface, zero top of atmosphere net radiation, and constant long-term average temperatures or  
436 tracer mass within each component. In reality however models are not perfectly conservative due to the limitations of numerical  
437 representation (i.e. machine precision) as well as possible design flaws or bugs in the code, and models are generally not run  
438 to perfect equilibrium due to computational constraints. Despite imperfect conservation or spin up, models can still usefully  
439 be applied, as long as the drifts in the control run are small relative to the signal of interest, in our case historical anthropogenic  
440 climate. Below we consider conservation and drift of heat, water and carbon in CanESM5 (Fig. 5).





441  
 442



443  
 444  
 445  
 446  
 447  
 448  
 449  
 450

**Figure 5: Stability of the CanESM5 piControl run, showing (a) top of atmosphere net heat flux, (b) net heat flux at the surface of ocean; (c) volume averaged ocean temperature; (d) global mean screen temperature; (e) net freshwater input at the liquid ocean surface; (f) dynamic sea level; (g) global sea-ice volume; (h) global snow mass; (i) land-atmosphere carbon flux; (j) ocean-atmosphere carbon flux. Heat fluxes in (a) and (b) are reported per metre squared of global area. The orange line in (b) is the heat flux computed at the bottom of the atmosphere, while the grey line is the heat flux computed at the surface of the liquid ocean (below sea-ice).**

The CanESM5 pre-industrial control shows a stable Top of Atmosphere (TOA) net heat flux of  $0.1 \text{ W m}^{-2}$  (fluxes positive down in  $\text{m}^2$  of global area, Fig. 5a). The model is close to radiative equilibrium and this control net TOA heat flux is over an order of magnitude smaller than the signal expected from historical anthropogenic forcing ( $>1 \text{ W m}^{-2}$ ). The global mean screen temperature is stable at around  $13.4^\circ\text{C}$  (Fig. 5d), indicating thermal equilibrium, and approximately in line with estimates of



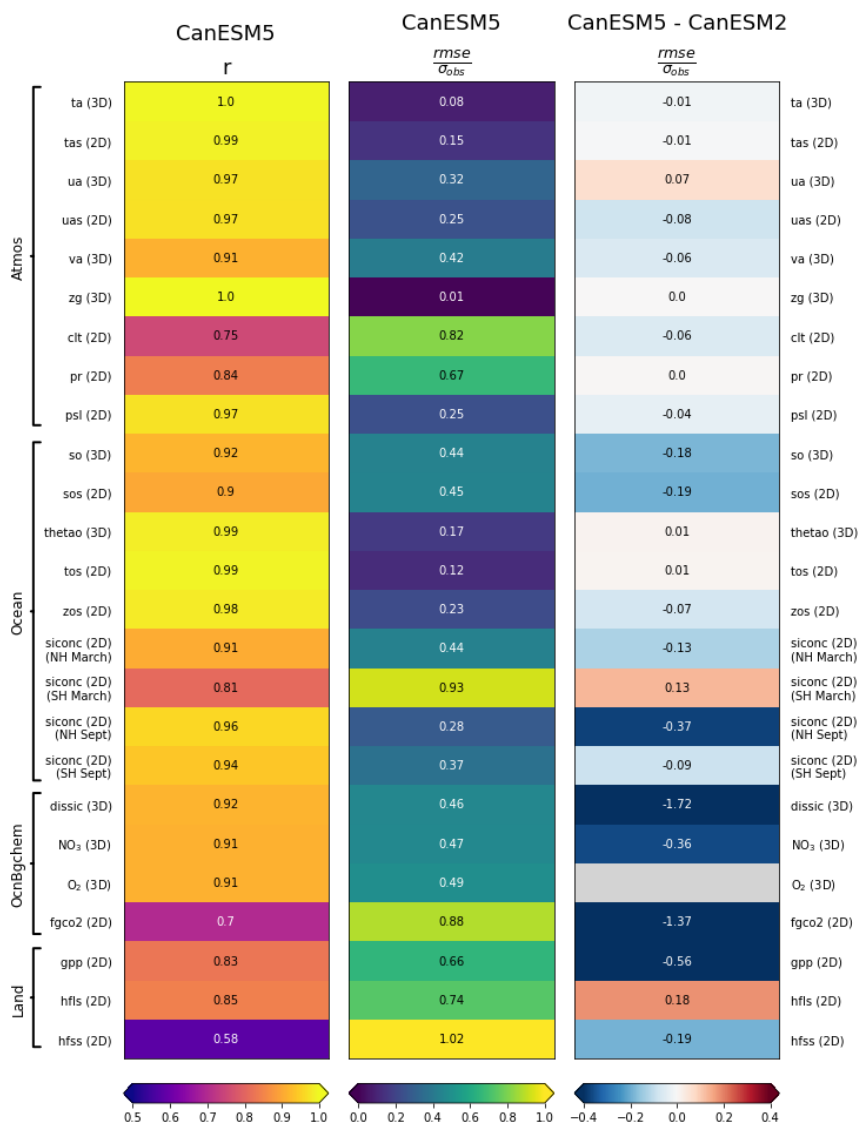
455 the temperature in 1850. Half of the net TOA flux is passed from the atmosphere to the ocean ( $0.05 \text{ Wm}^{-2}$ , Fig. 5b). With the  
456 conservative remapping in the coupler, the fluxes exchanged between components are identical to machine precision. However,  
457 the net heat flux received at the surface of the liquid ocean is  $0.14 \text{ Wm}^{-2}$ , almost three times higher than the heat flux passed  
458 from CanAM to NEMO (Fig. 5b). This discrepancy reflects a non-conservation of heat within the LIM2 ice model. Tests with  
459 an ice-free ocean do not suffer this problem. Nonetheless, the discrepancy is relatively small, and ice volume is stable. A  
460 further non-conservation occurs within the NEMO liquid ocean. Although the ocean receives a net heat flux of  $0.14 \text{ Wm}^{-2}$ , the  
461 volume averaged ocean is cooling at a rate equivalent to a flux of  $0.05 \text{ Wm}^{-2}$  (Fig. 5c) implying a total non-conservation of  
462 heat in the liquid ocean of about  $0.2 \text{ Wm}^{-2}$ . Conservation errors of this order are well known in NEMO v3.4.1, likely arise  
463 from the use of the linear free surface (Madec et al., 2012), and have been seen in previous coupled models using NEMO  
464 (Hewitt et al., 2011). Despite this, the volume averaged ocean temperature drift in CanESM5 is about half the size of the drift  
465 in CanESM2. Furthermore the lack of ocean heat conservation in CanESM5 is roughly constant in time, and appears to be  
466 independent of the climate (not shown).

467  
468 At the liquid ocean surface, a small net freshwater flux results in a freshening trend, and a sea-level rise of about 24 cm over  
469 1,000 years (Fig. 5e, f). This rate of drift is more than 20 times smaller than the signal of anthropogenic sea-level rise. The  
470 LIM2 ice model appears to be the source of non-conservation: the net freshwater flux provided from CanAM is very close to  
471 zero, about six times smaller than that noted above ( $24 \text{ cm} / 1000 \text{ years}$ ). Snow and ice volume are stable, not exhibiting any  
472 long term drift, yet they are subject to considerable decadal and centennial scale variability (Fig. 5g, h).

473  
474 Atmosphere-land carbon fluxes average to zero, and carbon pools within CTEM are stable (Fig. 5i, k). The net ocean carbon  
475 flux is fairly close to zero, but remains slightly negative on average at  $-0.02 \text{ Pg yr}^{-1}$  despite a multi-millennial spin up (Fig. 5j).  
476 The total mass of dissolved inorganic carbon in the ocean decreases very slightly as a result (Fig. 5l). The rate of ocean carbon  
477 drift is approximately an order of magnitude smaller than the modern day anthropogenic signal of ocean carbon uptake ( $>2 \text{ Pg}$   
478  $\text{yr}^{-1}$ ). The drifts identified above are all far smaller than would be expected from anthropogenically forced trends, confirming  
479 that the model is suitably stable to evaluate centennial scale climate change. In the following section, we consider the ability  
480 of the model to reproduce large scale features of the observed historical climate.

## 481 **5 Evaluation of historical mean climate**

482 In this section we use the CMIP6 historical simulations (Eyring et al., 2016) of CanESM5 “p1”, focusing on climatologies  
483 computed over 1981 to 2010, unless otherwise noted.



484  
 485  
 486  
 487  
 488  
 489

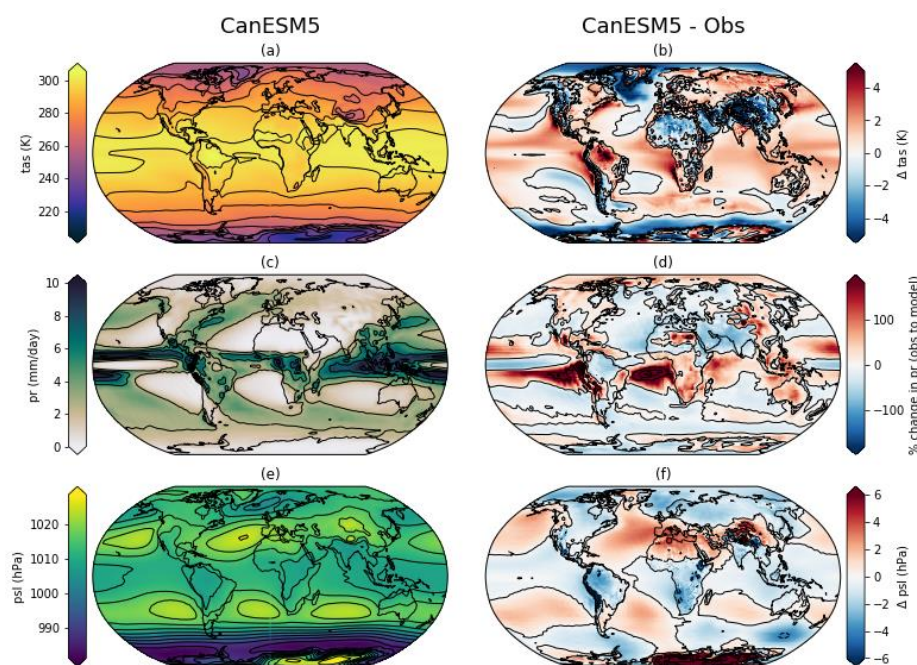
**Figure 6: Summary statistics quantifying the ability of CanESM to reproduce large scale climate features. Shown are the correlation coefficient ( $r$ ) between the simulated and observed spatial patterns, the Root Mean Square Error (RMSE) normalized by the (observed spatial) standard deviation ( $\sigma$ ), and the difference in normalized RMSE between CanESM5 and CanESM2. The spatial quantities represent temporal means over 1981 to 2010, except as noted in appendix F. Variables are labelled according to the names in the CMIP6 data request.**



## 490 5.1 Overall skill measures

491 The ability of CanESM5 to reproduce observed large scale spatial patterns in the climate system is quantified using global  
492 summary statistics computed over the 1981 to 2010 mean climate (Fig. 6). Shown are the correlation coefficient between  
493 CanESM5 and observations ( $r$ ), the Root Mean Square Error (RMSE) normalized by the observed (spatial) standard deviation  
494 ( $\sigma$ ), and the change in normalized RMSE between CanESM2 and CanESM5. The statistics are weighted by grid cell area for  
495 2D fields, volume for 3D ocean fields, and by area and pressure for 3D atmospheric variables. In general CanESM5  
496 successfully reproduces many observed spatial patterns of the surface climate, interior ocean, and the atmosphere, with  
497 correlation coefficients between the model and observations generally above 0.8. Some exceptions are the total cloud fraction  
498 ( $clt$ ,  $r=0.75$ ), atmosphere-ocean  $CO_2$  flux ( $fgco2$ ,  $r=0.7$ ) and the surface sensible heat flux ( $hfss$ ,  $r=0.58$ ).

499 For most variables, normalized RMSE has decreased in CanESM5 relative to CanESM2, indicating an improvement in the  
500 ability of the new model to reproduce observed climate patterns over its predecessor. The largest improvements were seen for  
501 ocean biogeochemistry variables, while small increases in error were seen for 3D distribution of zonal winds ( $ua$ ), sea surface  
502 temperatures ( $tos$ ), the March distribution of sea-ice in the Southern Hemisphere ( $siconc$ ), and surface latent heat flux ( $hfls$ ).  
503 In the following sections individual realms are examined, with a closer look at regional details and biases.



504

505

506

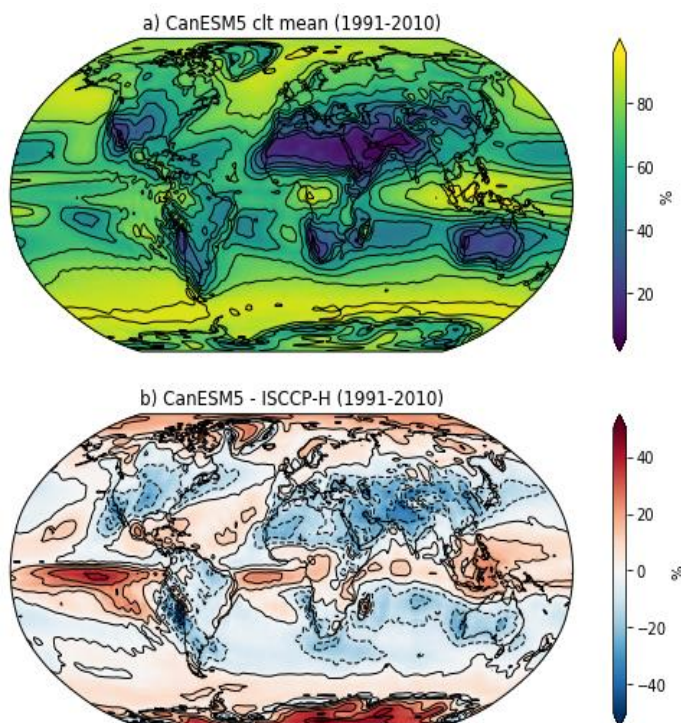
507

**Figure 7: Climatologies over 1981 to 2010 of (a) surface air temperature, (c) precipitation and (e) sea-level pressure in CanESM5, and their bias from (b) ERA5, (d) GPCP and (f) ERA5 over the same period.**



508 **5.2 Atmosphere**

509 CanESM5 reproduces the large scale climatological features of surface air temperatures, precipitation and sea-level pressure,  
510 though significant regional biases exist (Fig. 7). CanESM5 is significantly colder than observed over sea-ice covered regions  
511 (Fig. 7a, b), noticeable in the Southern Ocean, and most obviously in the region surrounding the Labrador sea, which has  
512 extensive seasonal sea-ice cover in CanESM5 (see below). The Tibetan plateau, the Sahara and the broader North Atlantic  
513 Ocean are also cooler than observed. Warm biases exist over the eastern boundary current systems (Benguela, Humboldt, and  
514 California); over the Amazon, eastern North America, much of Siberia, and over broad regions of the tropical and subtropical  
515 oceans.



516  
517 **Figure 8: Cloud fraction in (a) CanESM5 and (b) the bias with respect to ISCCP-H satellite based**  
518 **observations.**  
519

520 Precipitation biases vary in sign by region (Fig. 7d). The largest relative (to mean) biases are excessive simulated precipitation  
521 over the eastern Pacific and Atlantic oceans, between the equator and extending into the southern subtropics. The largest land  
522 biases are excessive precipitation over much of sub-Saharan Africa, Southeast Asia, Canada, and Peru-Chile. In contrast  
523 western Asia, Europe, the North Atlantic and the subtropical to high-latitude Southern Oceans have too little simulated  
524 precipitation. The large scale pattern of sea-level pressure is captured by CanESM5 (Fig. 7e). Biases relative to ERA5 are

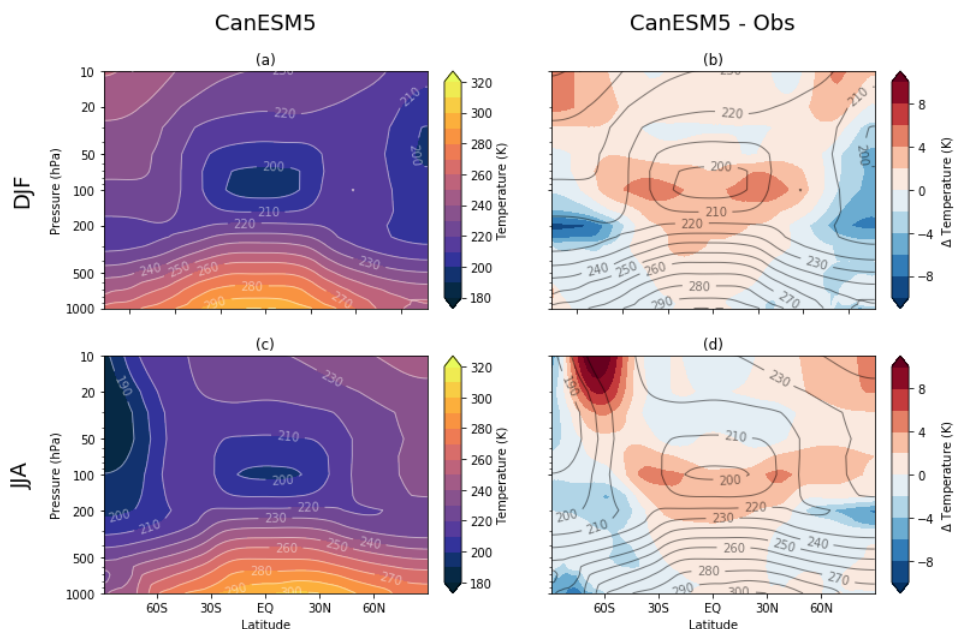


525 largest over the high elevations of Antarctica (Fig. 7f), possibly reflecting differences in the extrapolation of surface pressure  
526 to sea-level.

527  
528 Relative to ISCCP-H (Young et al, 2018), version 1.00 (Rossow et al, 2016) the total cloud fraction in CanESM5 is  
529 overestimated along the equator, particularly in the eastern tropical Pacific (Fig 8). Too large cloud fraction is also found over  
530 Antarctica and the Arctic. Underestimates of total cloud fraction occur over most other land areas, with the largest  
531 underestimates over Asia and the Himalayas.

532  
533 Zonal mean sections of air temperature for the DJF and JJA seasonal means are shown in Fig. 9. In both seasons, CanESM5  
534 is biased warm relative to ERA5 near the tropopause, across the tropics and subtropics. Warm biases also occur in the  
535 stratosphere, notably near 60°S above 50 hPa in JJA. Cold biases exist from the subtropics to the high latitudes, where they  
536 reach from the surface to the stratosphere, and are strongest in the winter season.

537  
538



539  
540 **Figure 9: Zonal mean temperature in CanESM5 (a, c) and bias relative to ERA5 (b, d) over 1981-2010, for**  
541 **the DJF (a, b) and JJA (c, d) seasons.**

542

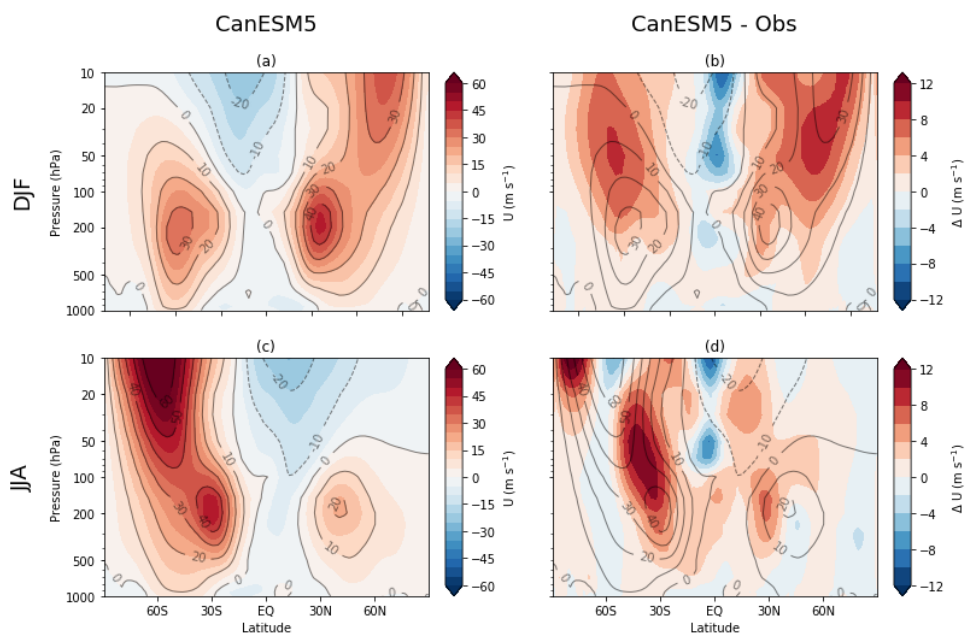


**Figure 10: Zonal mean zonal winds (a, c) and bias relative to ERA5 (b, d) over 1981-2010, for the DJF (a, b) and JJA (c, d) seasons.**

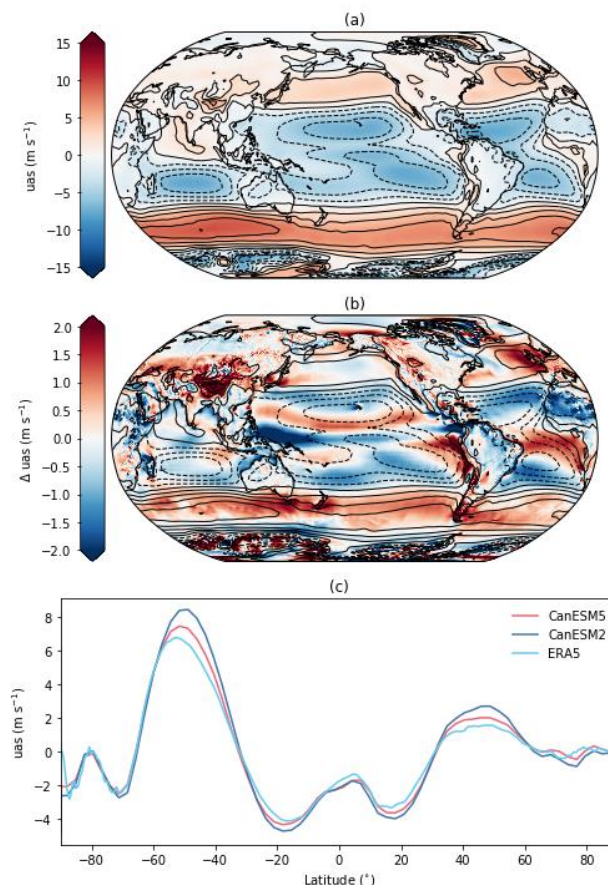
Zonal mean zonal winds are compared to ERA5 in Fig. 10 for DJF and JJA. The westerly jets in CanESM5 are biased strong, particularly aloft and in the winter hemisphere. Surface zonal winds in CanESM5 are only slightly stronger than observed, and are significantly improved over those in CanESM2 (Fig. 11), which were too strong, particularly over the Southern Hemisphere westerly jet.

### 5.3 Land physics and biogeochemistry

Figures 12 and 13 compare the geographical distribution and zonal averages of gross primary productivity (GPP), and latent and sensible heat fluxes over land with observation-based estimates from Jung et al. (2009). The zonal averages of GPP, and latent and sensible heat fluxes compare reasonably well with observation-based estimates although the latent heat fluxes are somewhat higher especially in the southern hemisphere as discussed below (Fig. 13). Figure 12 shows the biases in the simulated geographical distribution of these quantities. In the tropics biases in GPP, and latent and sensible heat fluxes, broadly correspond to biases in simulated precipitation compared to observation-based estimates (shown in Fig. 7).



563



564

565

**Figure 11: Zonal surface winds in (a) CanESM5, (b) the bias relative to ERA5 and (c) zonal-mean zonal surface winds in CanESM2, CanESM5 and ERA5.**

566

567

568

569

570

571

572

573

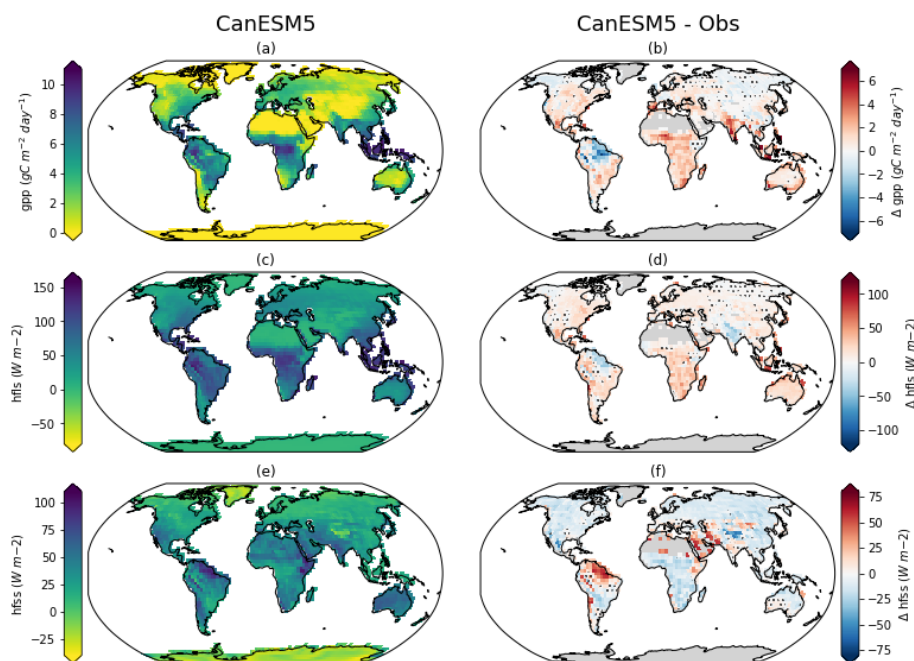
574

575

576

Generally over tropics, as would be intuitively expected, the sign of GPP and latent heat flux anomalies are the same since they are both affected by precipitation in the same way. Sensible heat flux is expected to behave in the opposite direction compared to GPP and latent heat flux in response to precipitation biases. For example, simulated GPP and latent heat fluxes are lower, and sensible heat fluxes higher in the north eastern Amazonian region because simulated precipitation is biased low (Fig. 7). The opposite is true for almost the entire African region south of the Sahara desert and most of Australia. Here simulated precipitation that is biased high, compared to observations, results in simulated GPP and latent heat flux that are higher and sensible heat flux that is lower than observation-based estimates. At higher latitudes, where GPP and latent heat flux are limited by temperature and available energy, the biases in precipitation do not translate directly into biases in GPP and latent heat flux as they do in the tropics.





577

578

579

580

581

582

583

584

585

586

587

588

589

590

591

592

593

594

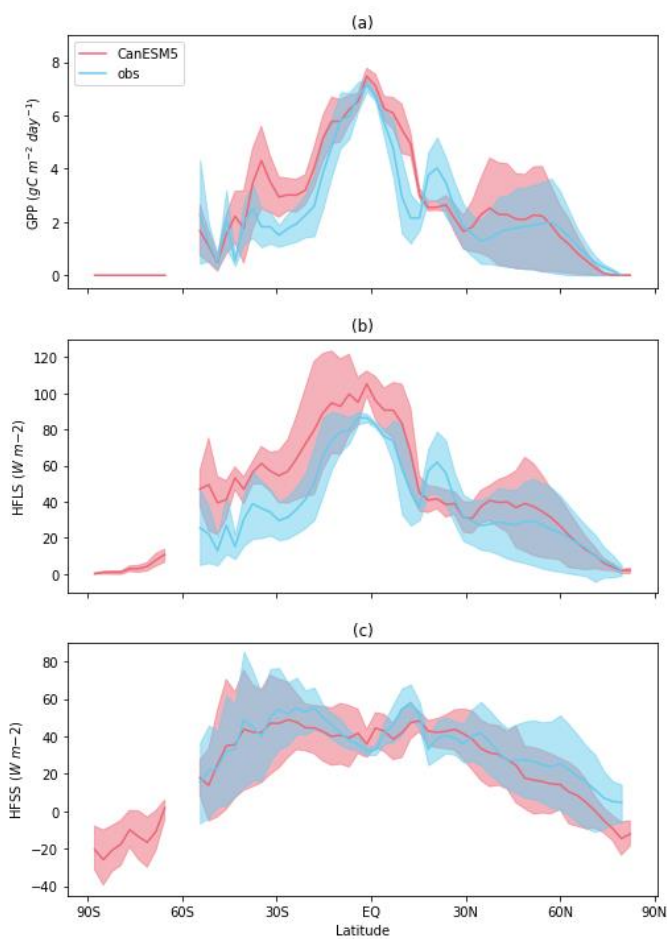
595

**Figure 12: Time-mean values of (a) gross primary productivity (GPP), (c) latent heat flux (HFLS), and (e) sensible heat flux (HFSS) from CanESM5 (r1i1p1f1) (left-hand column) and the corresponding biases with respect to observation-based reference data presented in Jung et al. (2009) (GBAF) (right-hand column). Black dots mark grid cells where biases are not statistically significant at the 5% level using the two-sample Wilcoxon test.**

The biases in simulated climate imply that simulated land surface quantities will also be biased which make it difficult to assess if the underlying model behaviour is realistic. This limitation can be alleviated to some extent by looking at the functional relationships between a quantity and its primary climate drivers. This technique works best when a land component is driven offline with meteorological data. In a coupled model, as is the case here, land-atmosphere feedbacks can potentially worsen a model's performance by exaggerating an initial bias. For example, low model precipitation can be further reduced due to feedbacks from reduced evapotranspiration some of which is recycled back into precipitation. Figure 14 shows the functional relationships between GPP and temperature, and GPP and precipitation, for both model and observation-based estimates. The observations-based temperature and precipitation data used in these plots are from CRU-JRA reanalysis data that were drive participating terrestrial ecosystem models in the TRENDY Intercomparison for the 2018 Global Carbon Budget (Le Quéré et al., 2018). Figure 14 shows that GPP increases both with increases in precipitation (as would be normally expected) and temperature except at mean annual values above 25 °C when soil moisture limits any further increases. This threshold emerges both in the model and the observation-based functional relationships. With the caveat mentioned above, the functional relationships of GPP with temperature and precipitation based on simulated data compare reasonably well with those based on



596 observation-based data, although the simulated GPP relationship with precipitation compares much better to its observation-  
597 based relationship than that for temperature.  
598



599  
600 **Figure 13: Zonal mean values of (a) GPP, (b) HFLS, and (c) HFSS for CanESM5 (r1i1p1f1) (black) and reference**  
601 **data (red) from Jung et al. (2009). The shading presents the corresponding inter-quartile range (IQR).**

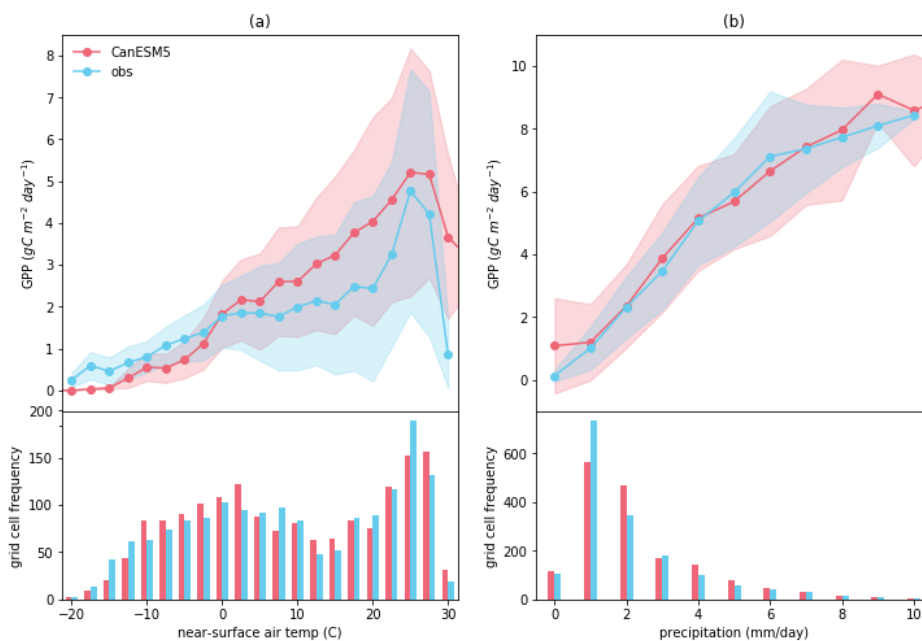


**Figure 14: Functional response of GPP to (a) near-surface air temperature and (b) surface precipitation for CanESM5 (r1i1p1f1) (black) and reference data (red) from Jung et al. (2009) (GBAF). The shading presents the corresponding standard deviation. The grid cell frequencies are shown in the lower part of each plot.**

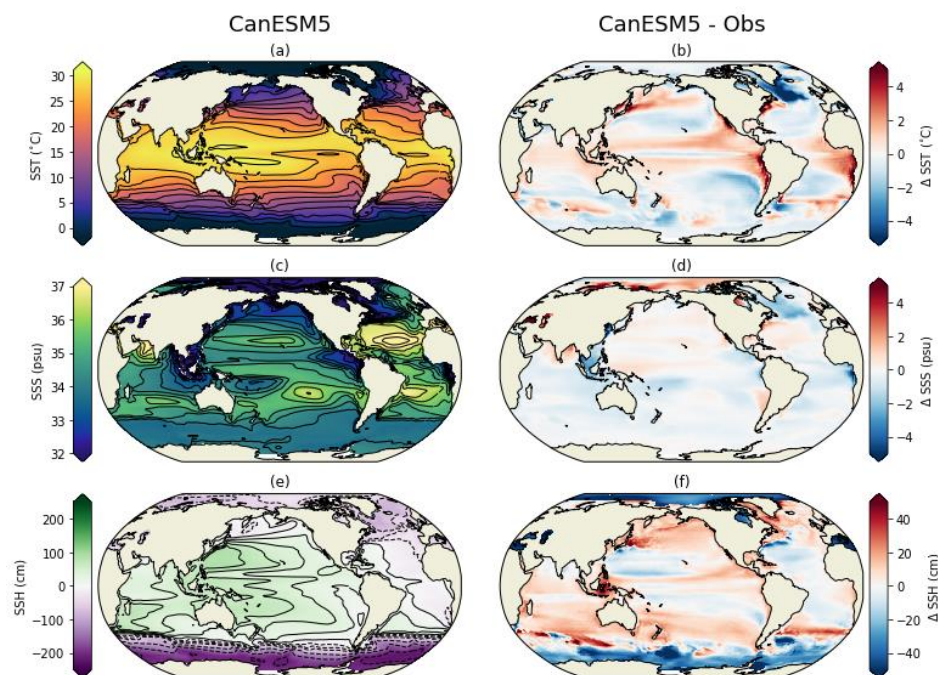
#### 5.4 Physical ocean

CanESM5 reproduces the observed large scale features of sea surface temperature (SST), salinity (SSS) and height (SSH) (Fig. 15). The largest SST biases are the cold anomalies south east of Greenland and in the Labrador Sea (Fig. 15b). These negative SST biases are associated with excessive sea-ice cover, described further below, and with the surface air temperature biases mentioned above. Positive SST biases are largest in the Eastern Boundary Current upwelling systems, as for surface air temperatures.

Sea surface salinity biases are largest, and positive, around the Arctic coastline, potentially indicating insufficient runoff in this region (Fig. 15d). Negative annual mean SSS biases occur under the region associated with excessive March sea-ice in the Labrador Sea, and are also found in seas of the maritime continent. Sea-surface height (SSH) is shown as an anomaly from the (arbitrary) global mean (Fig. 15e). Significant SSH biases are associated with the positions of western boundary currents, noticeably for the Gulf Stream and Kuroshio current (Fig. 15f). CanESM5 has too low SSH around Antarctica, and too high SSH in the southern subtropics, with an excessive SSH gradient across the Southern Ocean. This SSH gradient is associated with the geostrophic flow of the Antarctic Circumpolar Current (ACC). The ACC in CanESM5 is vigorous with 190 Sv of transport through Drake Passage. This is larger than observational estimates which range up to 173.3 +/- 10.7 Sv (Donohue et



622 al, 2016). In CanESM5 the ACC also exhibits a pronounced, centennial scale variability of about 20 Sv, which is also evident  
623 in the piControl simulation (not shown).  
624



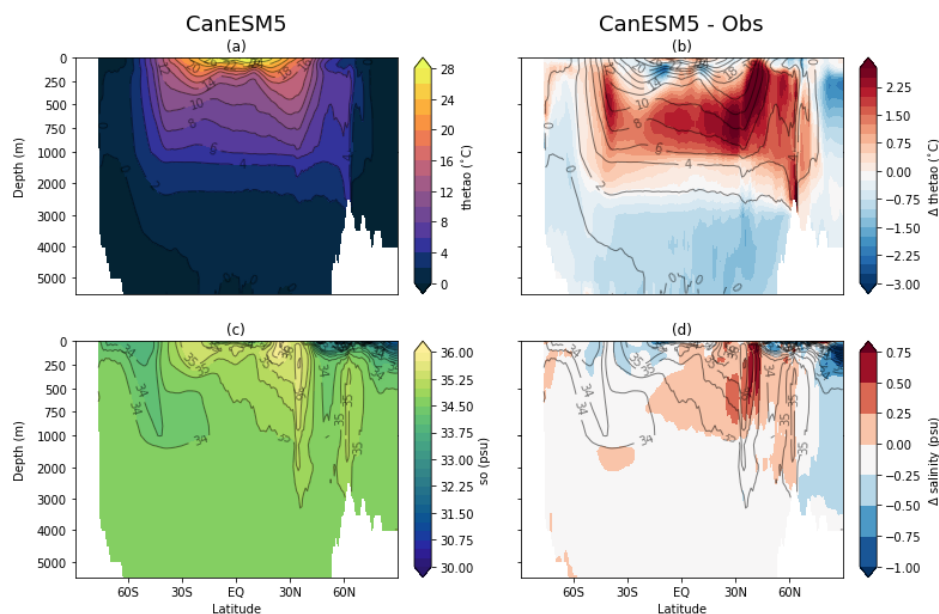
625  
626 **Figure 15. Sea surface (a) temperature, (c) salinity and (e) height averaged over 1981 to 2010, and their biases relative**  
627 **to World Ocean Atlas 2009 (b, d), and the AVISO mean dynamic topography (f).**  
628

629 The CanESM5 interior distributions of potential temperature and salinity are well correlated with observations (Fig. 6). In the  
630 zonal mean, potential temperature biases are largest within the thermocline, which is warmer than observed, particularly near  
631 50°N (Fig. 16a, b). The deep ocean, the Southern Ocean south of 50°S and the Arctic Ocean are cooler than observed. The  
632 pattern of excessive heat accumulation in the thermocline is very similar to the pattern of bias seen in CMIP5 models on  
633 average (Flato et al., 2013 their Fig. 9.13). The major salinity bias is of excessive fresh waters in the Arctic near 250 m, also  
634 typical of the CMIP5 models (Fig. 16d). Sea-surface salinities showed the Arctic to be too salty, but this bias is confined to  
635 near the surface, and at all depths below the immediate surface layer the Arctic Ocean is too fresh. The zonal mean salinity  
636 also shows a positive salinity bias near 40°N, associated with the Mediterranean outflow.

637  
638 The Meridional Overturning Circulation in the global ocean, and the Indo-Pacific, as well and Arctic-Atlantic basins is shown  
639 in Fig. 17. The global overturning streamfunction shows the expected major features: an upper cell with clockwise rotation,  
640 connecting North Atlantic Deepwater formation to low latitude and Southern Ocean upwelling; a vigorous Deacon cell in the  
641 Southern Ocean (as a result of plotting in z-coordinates); a lower counter clockwise cell of Antarctic Bottom Water, and



642 vigorous near-surface cells in the subtropics. The upper cell overturning rate at 26°N in the Atlantic is estimated to be 17±4.4  
643 Sv from the RAPID observational array (McCarthy et al. 2015). CanESM5 produces an Atlantic overturning rate of 12.8 Sv  
644 at 26°N, below the mean but within the range measured by RAPID.  
645



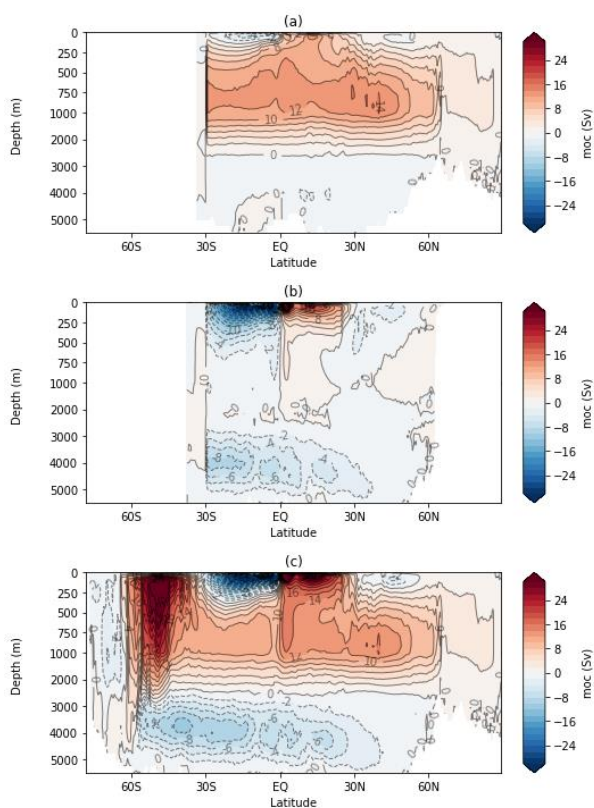
646  
647 **Figure 16: CanESM5 zonal mean ocean (a) potential temperature, (c) salinity averaged over 1981 to 2010, and their**  
648 **biases from World Ocean Atlas 2009 (b, d). Note the depth-scale on the y-axis is non-uniform.**

649  
650  
651  
652 Closely connected to the MOC is the rate of northward heat transport by the ocean (Fig. 18). CanESM5 produces the expected  
653 latitudinal distribution of heat transport, but consistent with a weak MOC, slightly underestimates the transport at 24°N, relative  
654 to the inverse estimate of Ganachaud and Wunsch (2003). To the north and south, CanESM5 ocean heat transport falls within  
655 the observational uncertainties. The MOC and heat transport in CanESM5 are similar to those in CanESM2, as reported in  
656 Yang and Saenko (2012)

657  
658  
659  
660  
661  
662



663



664

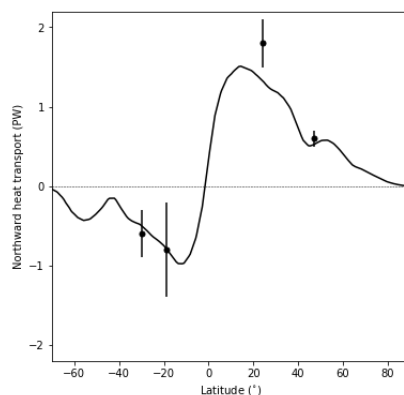
665

666

667

668

**Figure 17: CanESM5 residual meridional overturning circulation in the Atlantic (a), Indo-Pacific (b) and global (c) oceans, averaged over 1981 to 2010 including all resolved and parameterized advective processes. Note the depth-scale on the y-axis is non-uniform.**



669

670

671

**Figure 18: Northward heat transport in the global ocean in CanESM5 (in Petawatts), with error bars showing the inverse estimate of Ganachaud and Wunsch (2003).**

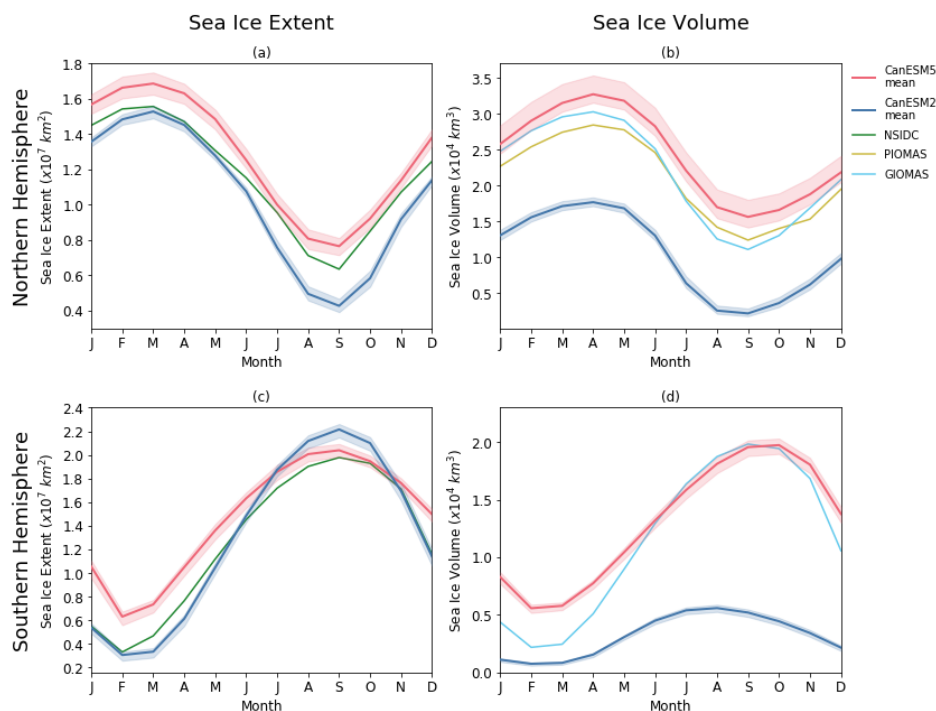


672

### 673 5.5 Sea-ice

674 The seasonal cycle of sea-ice extent and volume are shown in Fig. 19. A major change from CanESM2 is seen in the sea-ice  
675 volume (Fig. 19b, d). CanESM2 simulated very thin ice, and had about 40% less Northern Hemisphere (NH) ice volume than  
676 in the PIOMAS reanalysis. By contrast, CanESM5 has a larger NH ice volume than in CanESM2 and in PIOMAS (Fig. 19b).  
677 The amplitude and phase of the annual cycle in NH sea-ice volume in CanESM5 is similar to PIOMAS (Fig. 19b). In the  
678 Southern Hemisphere, CanESM5 also has a larger sea-ice volume and seasonal cycle far more consistent with the GIOMAS  
679 reanalysis product than CanESM2 (Fig. 19d).

680



681

682 **Figure 19: Seasonal cycles of sea-ice extent (a, c) and volume (b, d) in the Northern (a, b) and Southern (c, d)**  
683 **hemispheres averaged over 1981 to 2010. Results are shown for CanESM2, CanESM5, the NSIDC satellite based**  
684 **observations, and the PIOMAS and GIOMAS reanalyses.**

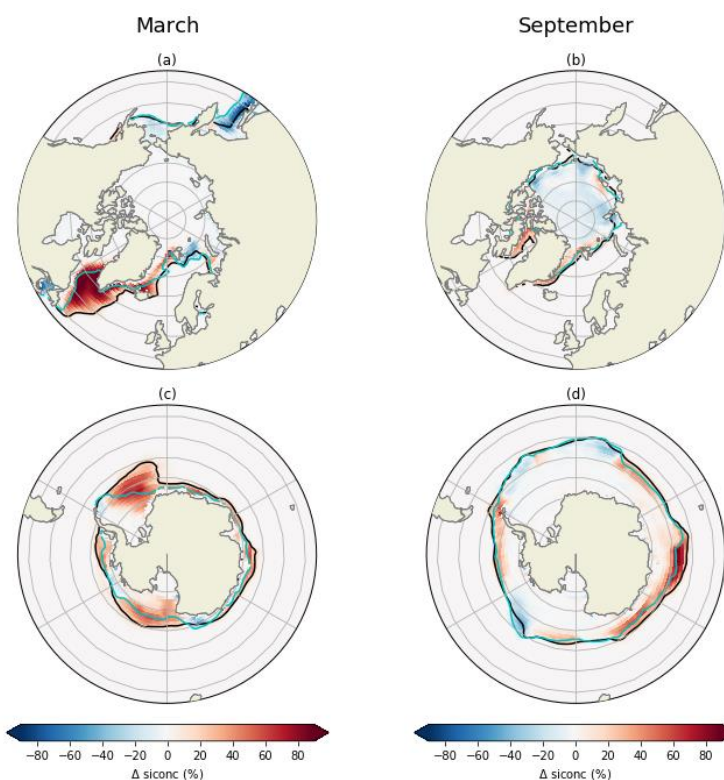
685

686

687 While CanESM2 significantly underestimated NH sea-ice extent relative to satellite based observations, CanESM5 generally  
688 overestimates the extent (Fig. 19a). The NH sea-ice extent biases are largest in the winter and spring. During the March  
689 maximum, excessive sea-ice is present in the Labrador Sea and east of Greenland (Fig. 20a). In the summer and fall, the net



690 NH extent bias is far smaller (Fig. 20c), and results from a cancellation between lower than observed concentrations over the  
691 Arctic basin and larger than observed concentrations around northeastern Greenland. Southern Hemisphere sea-ice extent  
692 biases are largest during the early months of the year, and in March the positive concentration biases are focused in the  
693 northeastern Weddell and Ross Seas (Fig. 20b). In September SH concentration biases between CanESM5 and the satellite  
694 observations are focused around the northern ice-edge, and are of varying sign (Fig. 20d).  
695



696  
697 **Figure 20: Sea-ice concentration biases between CanESM5 and NSIDC climatologies for the months of March (a, c)**  
698 **and September (b, d), in the Northern (a, b) and Southern (c, d) hemispheres. The solid black contour marks the ice-**  
699 **edge (15% threshold) in CanESM5, and the teal line marks the ice-edge in the observations. Biases are based on the**  
700 **1981 to 2010 climatology.**  
701

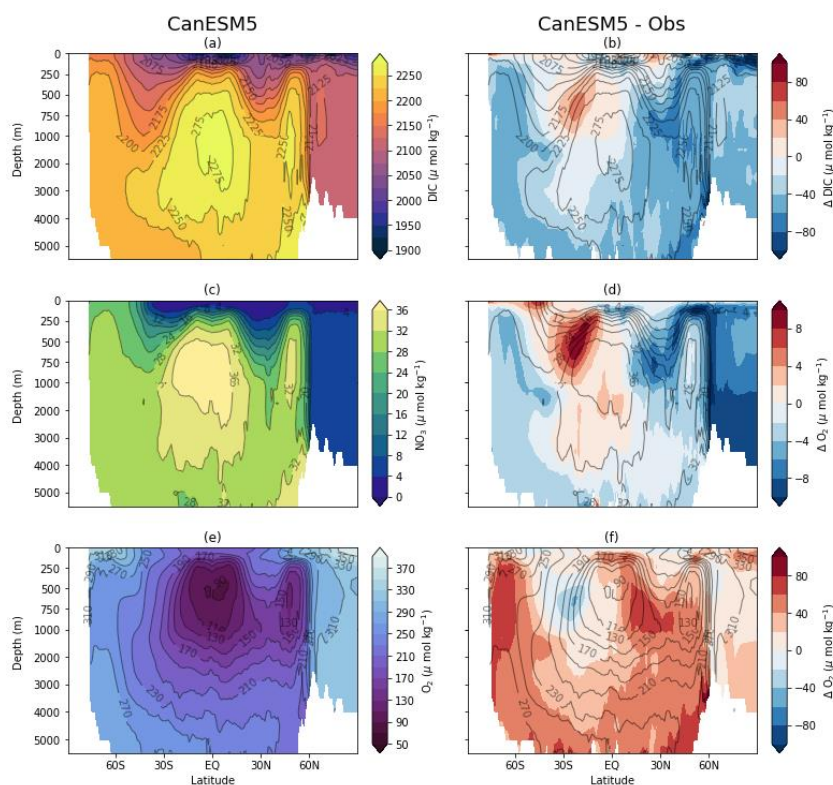
## 702 5.6 Ocean biogeochemistry

703 The standard configuration of CanESM5 has a significantly improved representation of the distribution of ocean  
704 biogeochemical tracers relative to CanESM2, despite using the same biogeochemical model (CMOC). For the three-  
705 dimensional distributions of Dissolved Inorganic Carbon (DIC) and NO<sub>3</sub>, and the surface CO<sub>2</sub> flux, the Root Mean Square





706 Error (RMSE), relative to observed distributions was reduced by over a factor of two (Fig.6). Ocean only simulations, whereby  
707 NEMO was driven by CanESM2 surface forcing via bulk formulae, show similar skill to the CanESM5 coupled model. From  
708 this we infer that changes in interior ocean circulation, rather than boundary forcing, are responsible for the improved  
709 representation of biogeochemical tracer distributions.  
710

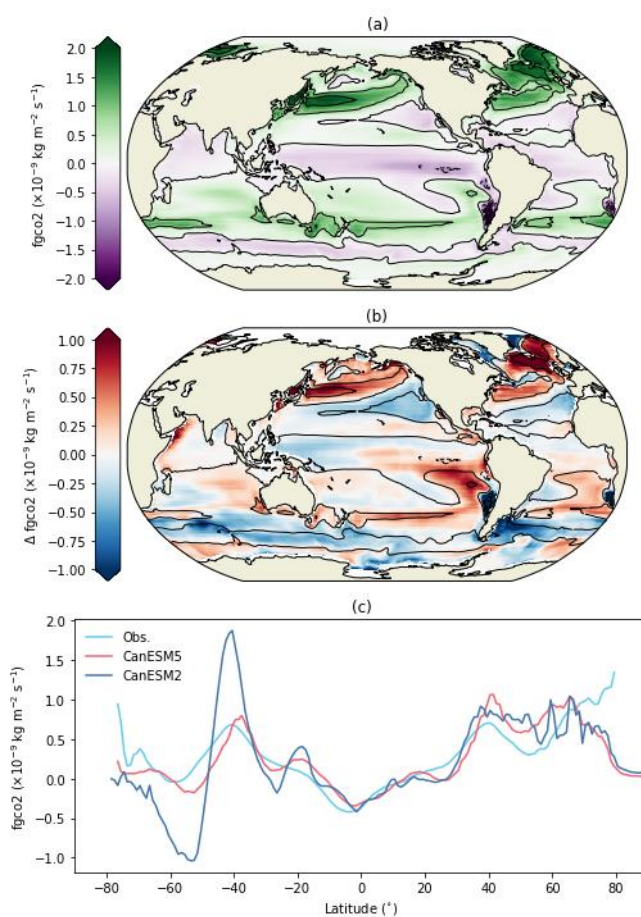


711  
712 **Figure 21: Zonal mean sections of (a) Dissolved Inorganic Carbon, (c) NO<sub>3</sub>, and (e) O<sub>2</sub> in CanESM5 averaged over**  
713 **1981 to 2010, and their biases relative to GLODAP v2 (b, d, f). Note the depth-scale on the y-axis is non-uniform.**  
714

715 In CanESM5 the zonal mean DIC concentration simulated by CMOC is generally lower than observed, by amounts reaching  
716 up to about 5% (Fig. 21a, b). One exception to this is in the SH subtropical thermocline, on the northern flank of the Southern  
717 Ocean, which shows positive DIC biases between 250 and 1000 m. This area is also one of positive nitrate biases, whose  
718 magnitude is close to 30% (Fig. 21d). Elsewhere zonal-mean NO<sub>3</sub> concentrations are generally too low, particularly in the NH  
719 thermocline and the Arctic. CanESM5 has higher than observed concentrations of zonal mean O<sub>2</sub> (Fig. 21f). As expected from  
720 saturation, biases are largest in the Southern and abyssal ocean, where CanESM5 is colder than observed. However, positive  
721 O<sub>2</sub> biases also occur at the base of the thermocline in the NH, where CanESM5 is too warm, suggestive of a biological origin.  
722



723 The zonal mean  $\text{NO}_3$  biases identified at the thermocline level above are the result of partially cancelling biases between the  
724 Pacific and Atlantic basins (not shown). The Atlantic has negative  $\text{NO}_3$  biases, largest near 1000 m. Meanwhile, there is an  
725 excessive accumulation of  $\text{NO}_3$  centered at the base of the eastern Pacific thermocline. This buildup occurs due to the simplified  
726 parameterization of denitrification in CMOC. Within each vertical column, the amount of denitrification is set to balance the  
727 rate of nitrogen fixation, and is distributed vertically proportional to the detrital remineralization rate. In reality nitrogen  
728 fixation and denitrification are not constrained to balance within the water column at any one location, but rather denitrification  
729 proceeds within anoxic areas. A prognostic implementation of denitrification implemented into CanOE resolves this bias, and  
730 will be discussed further in an upcoming article within this special issue.  
731



732  
733 **Figure 22: Ocean atmosphere flux of  $\text{CO}_2$  in (a) CanESM5 averaged over 1981 to 2010 (b) from Landschutzer (2009),**  
734 **and (c) zonal mean  $\text{CO}_2$  flux in CanESM2, CanESM5 and Landschutzer (2009) data.**  
735  
736



737 The atmosphere-ocean CO<sub>2</sub> flux pattern in CanESM5 correlates significantly better with estimates of the observed flux than  
738 CanESM2 (Fig. 6). The largest departures from the observations are positive biases in the southeastern Pacific, northwest  
739 Pacific and northwest Atlantic (Fig. 22b). These are compensated by negative biases in the Southern Ocean and mid-latitude  
740 northeast Pacific. In the zonal mean, CanESM2 had a large flux dipole in the Southern Ocean, which is significantly reduced  
741 in CanESM5, and attributable to improved circulation in the new NEMO ocean model and a reduction in Southern Ocean wind  
742 speed biases in CanAM5 (Fig. 22c).

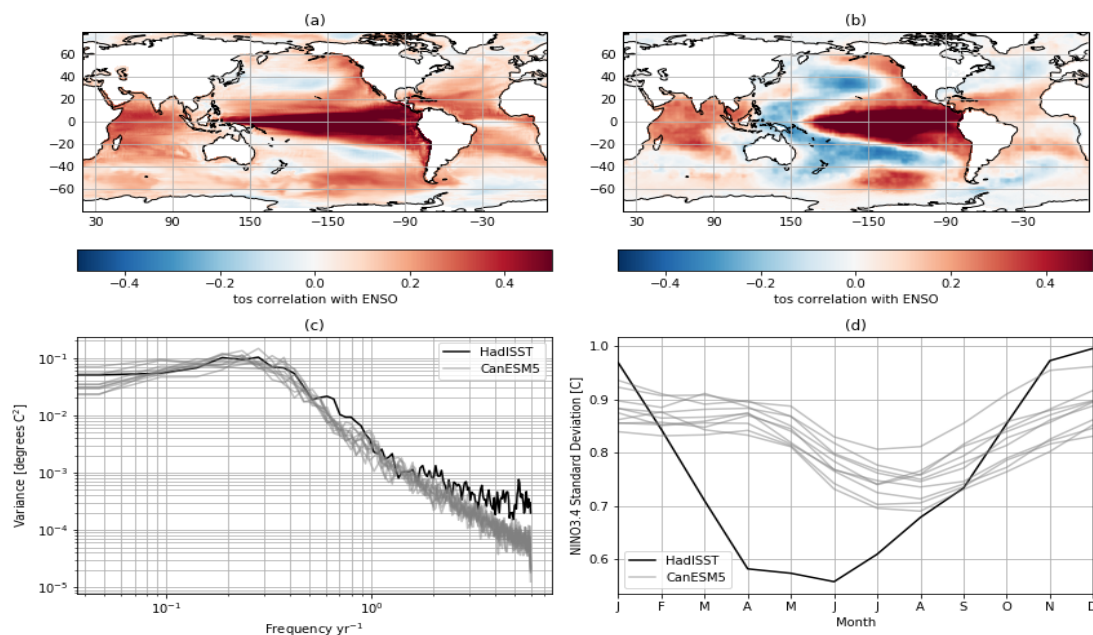
## 743 **5.7 Modes of climate variability**

### 744 **5.7.1 El-Niño Southern Oscillation**

745 The El-Niño Southern Oscillation (ENSO) is a key component of climate variability on seasonal and interannual timescales.  
746 To evaluate CanESM5's representation of ENSO, the NINO3.4 index (average monthly SST anomaly in the region bounded  
747 by 5S, 5N, 170W, 120W) from the first 10 historical ensemble members is compared against HadISST. The skill of CanESM5  
748 at representing the local and remote effects of ENSO is evaluated by correlating SST anomalies with the resulting NINO3.4  
749 index (Fig. 23a, b). Within the equatorial Pacific, a positive ENSO event in CanESM5 leads to an increase in SSTs across the  
750 entire basin whereas observations show negative SST anomalies in the western basin and positive anomalies in the central and  
751 eastern Pacific. ENSO in CanESM5 also has weaker teleconnections. The SST within the subtropical North and South Pacific  
752 gyres are more weakly anticorrelated to ENSO than observed. HadISST shows a negative North Atlantic Oscillation like  
753 pattern associated with ENSO, which is not present in CanESM5. The SST teleconnection in the tropical Indian and Atlantic  
754 Oceans is well represented by the model.

755  
756 The spectral peak in the historical ensemble members (Fig. 23c) occurs at around 3-5 years in general agreement with  
757 observations. Variability on decadal time-scales has a large spread between ensemble members likely due to differences in the  
758 strength of warming trends over the historical period. Higher frequency variability at monthly to seasonal timescales is  
759 significantly lower than observed. The lower monthly variability can also be seen by examining month-by-month interannual  
760 variability of NINO3.4 (Fig. 23d). While January remains the month of peak variability, overall the annual cycle of NINO3.4  
761 variability is weaker in CanESM5. In observations, ENSO variability is at its minimum between April and June but in  
762 CanESM5 the minimum variability (depending on the ensemble member) tends to be between July and September.

763  
764



765

766 **Figure 23: Characteristics of the El Niño Southern Oscillation (ENSO) from and the HadISST observational product.**

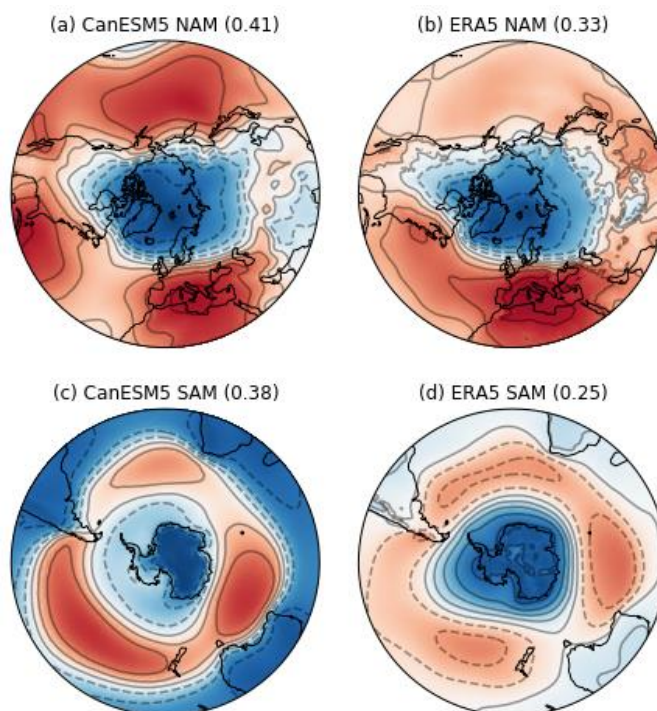
767 **Spatial maps in (a) and (b) are the regression of the SST monthly anomalies from 1850-2014 against the NINO3.4**  
768 **index from (a) CanESM5 (historical ensemble member r1i1p1f1) and (b) from HadISST. Temporal variability is**  
769 **summarized as power spectra (c) of the NINO3.4 index from HadISST and ten historical ensemble members and the**  
770 **interannual variability of the NINO3.4 index by month (panel d) for CanESM5 and HadISST.**

771

## 772 5.7.2 Annular Modes

773 The Northern Annular Mode is computed as the first EOF of extended winter (DJFM) sea level pressure north of 20°N for  
774 CanESM5 and ERA5 (Fig. 24 a, b). The correlation between the CanESM5 and ERA5 patterns is 0.95. Despite the high degree  
775 of coherence, some differences between the model pattern and reanalysis are evident (Fig. 24). For example CanESM5 has a  
776 positive centre in the north Pacific, not seen in ERA5, and the positive pattern across the North Atlantic is less continuous in  
777 CanESM5. This is a typical model bias (e.g. Bentson et al., 2013). The first EOF in CanESM5 also explains about 8% more  
778 variance than in the reanalysis.

779



780  
781 **Figure 24: First Empirical Orthogonal Functions (EOFs) of sea-level pressure north of 20N (a, b), and south of 20S (c,**  
782 **d), representing the Northern Annual Mode and Southern Annular Mode respectively. The NAM is based on the**  
783 **extended winter DJFM season, and the SAM is based on monthly sea-level pressure. Results are shown for CanESM5**  
784 **(a, c) and ERA5 (b, d), and the amount of variance explain by each EOF is given in brackets. The color scale is**  
785 **arbitrary.**

786  
787 The Southern Annular Mode is the dominant mode of climate variability in the Southern Hemisphere, with significant  
788 influences on atmospheric circulation, precipitation, and the Southern Ocean. We compute the SAM pattern as the first EOF  
789 of sea level pressure south of 20°S. The CanESM5 and ERA5 pattern correlation is 0.7. In CanESM5, the first EOF accounts  
790 for 13% more variance than in the reanalysis. Despite such biases, these results confirm that CanESM5 captures the principal  
791 modes of tropical and mid-latitude climate variability.

## 792 **6 Climate response to forcing**

### 793 **6.1 Response to CO<sub>2</sub> forcing**

794 The global mean screen temperature change under the idealized CMIP6 DECK experiments “abrupt-4xCO<sub>2</sub>” and “1pctCO<sub>2</sub>”  
795 are shown in Fig. 4. From these simulations, three major benchmarks of the model’s response to CO<sub>2</sub> forcing can be quantified  
796 (Table 3).



797 **Table 3: Key sensitivity metrics: Transient Climate Response (TCR), Transient Climate Response to Cumulative**  
798 **Emissions (TCRE), and Equilibrium Climate Sensitivity (ECS).**

Model	TCR (K)	TCRE (K/EgC)	ECS (K)
CanESM2	2.4	2.3	3.8
CanESM5	2.8	1.9	5.7

799

800

801 The Transient Climate Response (TCR) of the model is given by the temperature change in the 1pctCO<sub>2</sub> experiment, averaged  
802 over the 20 years centered on the year of CO<sub>2</sub> doubling (year 70), relative to the piControl. For CanESM5 the TCR is 2.8 K,  
803 an increase of 0.4 K over that seen in CanESM2. The CanESM5 TCR is larger than seen in any CMIP5 models, and  
804 significantly higher than the CMIP5 mean value of 1.8 K (Flato et al., 2013). The likely range ( $p > 0.66$ ) of TCR was given by  
805 the IPCC AR5 as 1.0-2.5 K (Collins et al., 2013), while more recent observational based estimates quote a 90% range of 1.2  
806 to 2.4 K (Schurer and Hegerl, 2018), again subject to significant observational and methodological uncertainty.

807

808 The Transient Climate Response to Cumulative Emissions (TCRE), incorporates the transient climate sensitivity together with  
809 the carbon sensitivity of the system (Mathews et al., 2009). It is defined as the ratio of global mean surface warming to  
810 cumulative carbon emissions, over the 20 years centered on CO<sub>2</sub> doubling in the 1pctCO<sub>2</sub> experiment, with units K EgC<sup>-1</sup>.  
811 The metric is of major policy relevance, and is widely used to estimate the allowable emissions to reach given temperature  
812 targets. The TCRE of CanESM5 is 1.9 K EgC<sup>-1</sup>, slightly lower than the CanESM2 value of 2.3 K EgC<sup>-1</sup>. The reduction in  
813 TCRE occurs despite the fact that CanESM5 has a larger temperature response (TCR) than CanESM2. The reduction occurs  
814 owing to significantly larger uptake of CO<sub>2</sub> by the land biosphere in CanESM5 relative to CanESM2 in the 1pctCO<sub>2</sub>  
815 experiment. Gillett et al. (2013) estimated the TCRE in 15 CMIP5 models to range from 0.8 to 2.4 K EgC<sup>-1</sup>, and the IPCC  
816 AR5 likely range was assessed as 0.8 to 2.5 K EgC<sup>-1</sup>.

817

818 The Equilibrium Climate Sensitivity (ECS) is defined as the amount of global mean surface warming resulting from a doubling  
819 of atmospheric CO<sub>2</sub>, and a key measure of the sensitivity to external forcing. Given the long equilibration time of the climate  
820 system, it is common to estimate ECS from the relationship between surface temperature change and radiative forcing, over  
821 the course of the first 140 years of the abrupt-4xCO<sub>2</sub> simulation (Gregory et al., 2004). For CanESM5, the ECS is 5.7 K, a  
822 significant increase over the value of 3.8 K in CanESM2. Like TCR, the CanESM5 ECS value is larger than seen in any CMIP5  
823 models, and significantly higher than the CMIP5 mean value of 3.2 K (Flato et al., 2013). The likely range for ECS was given  
824 by the IPCC AR5 as 1.5 to 4.5 K (Collins et al., 2013). CanESM5 falls outside this range, although it is worth noting that there  
825 are significant uncertainties in observational constraints of ECS. We also note, as above, that ECS is an emergent property in  
826 CanESM5 - no model tuning was done on the response to forcing.



827

828 A detailed explanation of the reasons behind the increased ECS in CanESM2 over CanESM5 is beyond the scope of this paper.  
829 However, the effective radiative forcing (Forster et al, 2016) in CanESM5 due to abrupt quadrupling of CO<sub>2</sub> is very similar to  
830 that in CanESM2, suggesting that changes in feedbacks rather than forcings are the source of the higher ECS. Indications are  
831 that the increase in ECS is associated with cloud and surface albedo feedbacks, with sea-ice likely playing an important role  
832 in the latter effect. A more detailed examination of the changes in ECS due to cloud microphysics will be provided in a  
833 companion paper in this special issue (Cole et al, 2019). The examination of climate change over the historical period in the  
834 following section also reveals some further insights.

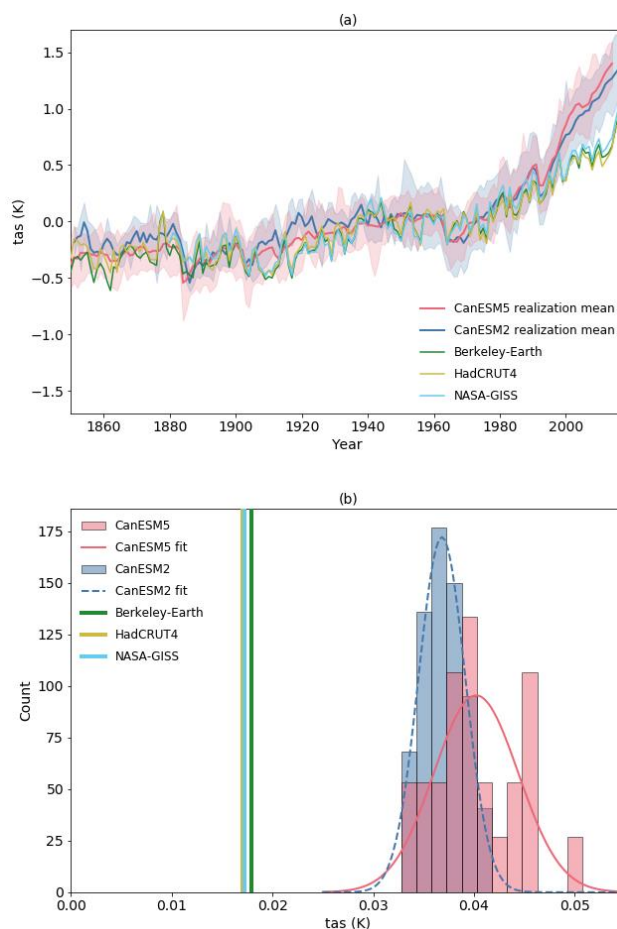
## 835 **6.2 Climate change over the historical period**

836 In this section we briefly discuss CanESM5 simulated changes in surface air temperature, sea-ice, and carbon cycle fluxes over  
837 the historical period. We choose these as major emblematic variables of climate change.

838

### 839 **6.2.1 Surface temperature changes**

840 Global Mean Screen Temperature (GMST) changes in CanESM2 and CanESM5 are generally consistent with the observations  
841 over the period from 1850 to around the end of the 20th century (Fig. 25a). However, from 2000 to 2014, the increase in GMST  
842 is larger in the models than observed. Possible reasons for the divergence are i) forcing errors in the CMIP5 and/or CMIP6  
843 forcing datasets, ii) natural internal variability, iii) incorrect partitioning of heat across components of the climate system or  
844 iv) a higher climate sensitivity in the model than in the real world. The 25 realizations of CanESM5 (and 50 realization of  
845 CanESM2) provide a good estimate the contribution of internal variability in the model. The observations fall outside the range  
846 of this variability, and hence this cannot account entirely for the divergence between the model and observations (assuming  
847 the model correctly captures the scale of internal variability). Trends computed from 1981 to 2014 show that the models are  
848 warming at roughly twice the observed rate over this period (Fig. 25b). The spread across the 25 realizations from CanESM5  
849 and 50 realizations from CanESM2 do not encompass the observations, reinforcing the point above. CanESM5 warms more  
850 rapidly than CanESM2 on average, as would be expected from its higher ECS and TCR. There is however significant overlap  
851 across the distribution of warming rates across the CanESM5 and CanESM2 ensembles. Interestingly, the lower tail of the  
852 trend probability distribution functions aligns for the two models, but CanESM5 has a broader distribution, and a larger tail of  
853 high warming realizations.



854

855 **Figure 25 (a) Global mean screen temperature in CanESM5, CanESM2 and various observational products and (b)**  
856 **histogram of historical trends over 1981 to 2014. In (a) the shaded envelopes represent the range over the CanESM2**  
857 **50 member large ensemble and the CanESM5 25 member “p1” ensemble. In (b) fits of the normal distribution to the**  
858 **CanESM2 and CanESM5 distributions are also shown.**

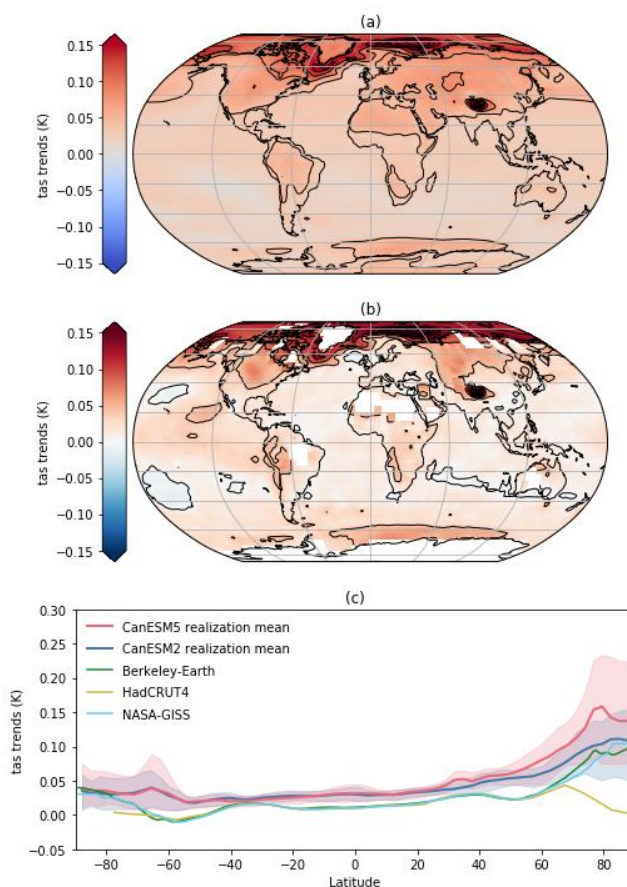
859

860 The pattern of surface warming in CanESM5 over the historical period is shown in Fig 26a. The canonical features of global  
861 warming are consistent between the model and observations: greater warming over land than ocean, and Arctic amplified  
862 warming. The zonal-mean warming trends (Fig 26c) show that both CanESM2 and CanESM5 warmed more than the  
863 observations over most latitudes. Divergence between simulated and observed warming rates is largest in the high latitudes,  
864 notably over the Southern Ocean and north of 40°N. The larger warming in the CanESM5 ensemble mean, relative to the  
865 CanESM2 ensemble mean, largely occurs over the Arctic. However, there is a very large variability in Arctic warming trends  
866 in CanESM5, which most likely are responsible for the spread in GMST trends noted above. Some realizations have lower  
867 trends, which overlap with observed warming, while others exhibit considerably higher rates of Arctic warming. Observed





868 warming rates over the Arctic are also some of the most uncertain, due to data sparsity (HadCRUT is masked where  
869 observations are not available).  
870



871  
872 **Figure 26: Surface temperature trends in CanESM5 (a), the difference in trend between CanESM5 and HadCRUT4**  
873 **(b), and zonal mean of trends in CanESM2, CanESM5, and HADCRUT4 over 1981 to 2014 (c). The shaded envelopes**  
874 **in (c) represent the range over the CanESM2 50 member large ensemble and the CanESM5 25 member “p1”**  
875 **ensembles.**

### 877 6.2.2 Sea-ice changes

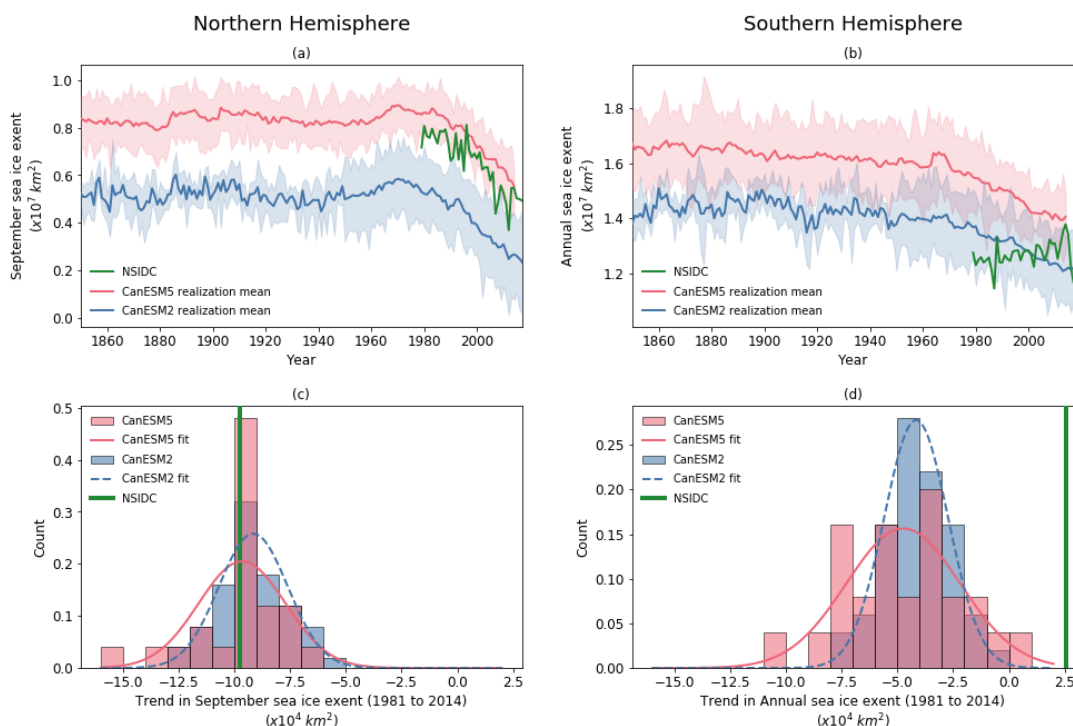
878 CanESM5 closely reproduces the observed reduction in Arctic September sea-ice extent (Fig. 27a). The trends from both the  
879 50 CanESM2 ensemble members, and the 25 CanESM5 ensemble members, show a broad spread due to internal variability  
880 (Fig. 27c). The observed trends lie close to the centre of the model distribution of trends. Given that CanESM5 warms more  
881 rapidly than observed, the sea-ice sensitivity (rate of sea-ice decline normalized by the rate of warming) is likely too low  
882 (Rosenblum and Eisenman, 2017; Winton, 2011).



883

884 In the Southern Hemisphere, observed annual mean Antarctic sea-ice extent showed a tendency to increase, before dramatic  
 885 declines in the past few years (Fig. 27b). Both CanESM5 and CanESM2 show consistent declines over the historical period,  
 886 with CanESM2 matching the climatological extent more closely. The spread of trends from the CanESM2 and CanESM5  
 887 ensembles suggest that the observed small positive trends in historical Antarctic sea-ice extent could plausibly have been due  
 888 to internal climate variability (Fig. 27d).

889



890

891 **Figure 27: Time series of sea-ice extent during (a) September in the Northern Hemisphere and (b) the annual mean in**  
 892 **the Southern Hemisphere in CanESM5, CanESM2, and NSIDC satellite based observations. The histogram of trends**  
 893 **over 1981 to 2014 in the lower panels. The shaded envelopes represent the range over the CanESM2 50 member large**  
 894 **ensemble and the CanESM5 25 member “p1” ensemble. Fits of the normal distribution to the CanESM2 and**  
 895 **CanESM5 histograms are also shown.**

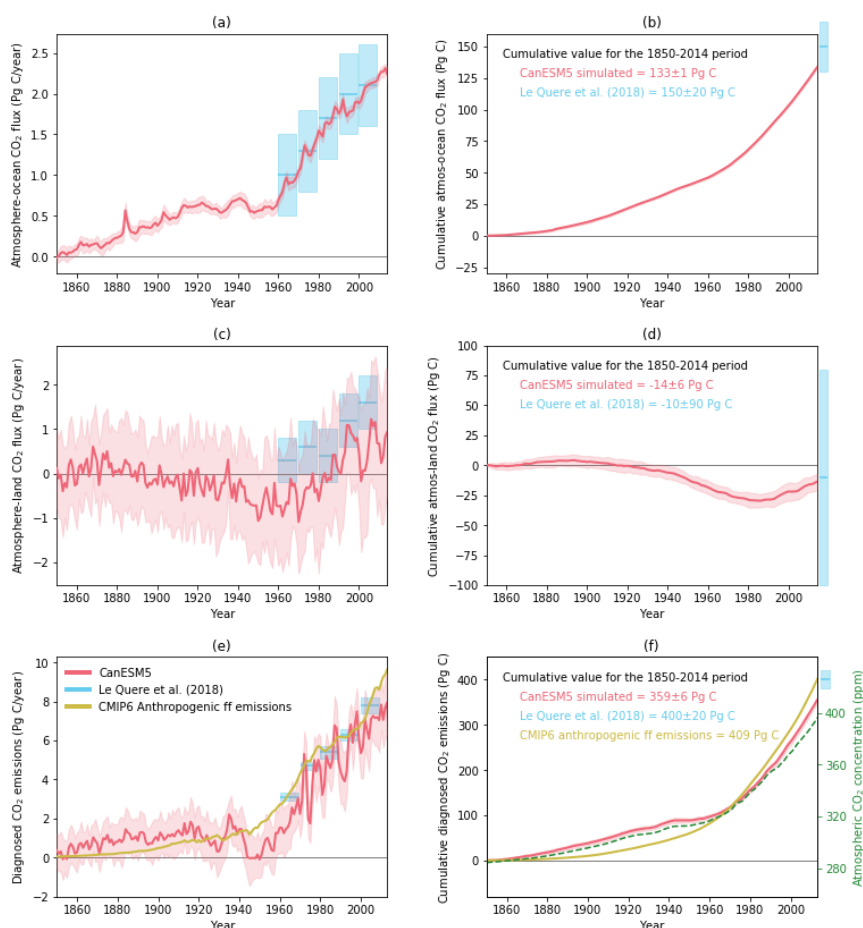
896

### 897 6.2.3 Historical carbon cycle changes

898 The simulated global atmosphere-ocean ( $F_O$ ) and atmosphere-land ( $F_L$ )  $CO_2$  fluxes are shown in Fig. 28 for the historical  
 899 period, along with their cumulative values over time. Also shown are the diagnosed anthropogenic fossil fuel emissions (E)  
 900 that are consistent with the specified  $CO_2$  pathway over the historical period, corrected for any drift in model’s pre-industrial



901 control simulation (see Appendix F). The simulated values of  $F_L$ ,  $F_O$ , and  $E$  are compared against estimates from the Global  
902 Carbon Project (Le Quéré et al., 2018).  
903



904  
905 **Figure 28: Annual (left column) and cumulative (right column) global values of simulated atmosphere-ocean and**  
906 **atmosphere-land CO<sub>2</sub> fluxes, and diagnosed anthropogenic fossil fuel emissions, shown in blue colour. The model**  
907 **values are shown as mean ± 1 standard deviation range and calculated based on the 25 ensemble members of the**  
908 **historical simulation. Model values are compared against estimates from Le Quere et al. (2018).**

909  
910  
911 In Fig. 28a the simulated global atmosphere-ocean CO<sub>2</sub> fluxes compares reasonably well with observation-based estimates  
912 from Le Quéré et al. (2018) for the decades of 1960s through to 2000s, although the simulated cumulative value of 133±1 Pg  
913 C for the 1850-2014 period is on the lower end of the observation-based estimate of 150±20 Pg C (Fig. 28b). In contrast, the  
914 simulated mean atmosphere-land CO<sub>2</sub> fluxes (Fig. 28c) are lower than their observation-based estimates for the decades of



915 1960s through to 2000s but their cumulative value of  $-14 \pm 6$  Pg C over the 1850-2014 period compares well with the  
916 observation-based estimate of  $-10 \pm 90$  Pg C (Fig. 28d). The caveat here, of course, is the large uncertainty range in the  
917 observation-based estimate of net cumulative atmosphere-land CO<sub>2</sub> flux (Appendix F). The reason the model's simulated  
918 cumulative uptake of  $-14 \pm 6$  Pg C over the 1850-2014 period compares well with the observation-based estimate of  $-10 \pm 90$   
919 Pg C, despite its weaker carbon sink since the 1960s (Fig. 28, panel c) is likely because the carbon source from land use change  
920 emissions is also lower.

921

922 Panel e and f in Fig. 28 show the allowable diagnosed fossil fuel emissions and their cumulative values for the 1850-2014  
923 period. The cumulative diagnosed fossil fuel emissions of  $359 \pm 6$  Pg C from the model for the period 1850-2014 are somewhat  
924 lower than the CMIP6 and Le Quéré et al. (2018) estimates of 409 and  $400 \pm 20$  Pg C, respectively.

## 925 **7 Conclusions**

926 CanESM5 is the latest coupled model from the Canadian Centre for Climate Modelling and Analysis. Relative to its  
927 predecessor, CanESM2, the model has new ocean, sea-ice and coupling components, and includes updates to the atmospheric  
928 and land surface. The model produces a stable pre-industrial control climate, and notwithstanding some significant biases,  
929 CanESM5 is able to reproduce many features of the historical climate. Objective global skill metrics show that CanESM5  
930 improves the simulation of observed large scale climate patterns, relative to CanESM2, for most variables surveyed. A notable  
931 feature of CanESM5 is its high equilibrium climate sensitivity of 5.7 K, an emergent property of the updated physics described  
932 above. This higher climate sensitivity appears to be driven by increased cloud and sea-ice albedo feedbacks in CanESM5. The  
933 first major science application of CanESM5 is for CMIP6, with over 50, 000 years of CanESM5 simulation and more than 100  
934 PB of data submitted to the publicly available CMIP6 archive. The model source code is also openly published for the first  
935 time. Going forward CanESM5 will continue to be used for climate science applications in Canada.

936

## 937 **8 Code availability**

938 The full CanESM5 source code is publicly available at <https://gitlab.com/ccma/canesm>. The version of the code which can  
939 be used to produce all the simulations submitted to CMIP6, and described in this manuscript, is tagged as v5.0.3, and has the  
940 associated DOI: [10.5281/zenodo.3251113](https://doi.org/10.5281/zenodo.3251113).

941

## 942 **9 Data availability**

943 All CanESM5 simulations conducted for CMIP6, including those described in this manuscript, are publicly available via the  
944 Earth System Grid Federation (ESGF). All observational data used is publicly available. Data sources and citations are  
945 provided in Appendix F.



946 **Appendices**

947 **Appendix A: Exchanges through the coupler**

948 **Table A1: Fields received by CanAM from CanCPL. The representative area may be the full AGCM grid cell (land,**  
 949 **ocean, and ice), “C”, open ocean, “O”, sea-ice, “I”, or the combination. Fields may be instantaneous, “Inst”, or averaged**  
 950 **over the coupling cycle, “avg”.**

Field Received	Field Description	Area	Avg
SICN_atm	sea ice fraction	OI	Inst
SIC_atm	ice water equivalent of sea ice	OI	Inst
SNO_atm	snow water equivalent over sea ice	I	Inst
GT_atm	sea surface temperature	O	Inst
CO2flx_atm	CO2 flux	OI	Inst

951

952 **Table A2 Fields sent from CanNEMO to CanCPL. Descriptions as in Table A1.**

Field Sent	Field Description	Area	Avg
OIceFrc	sea ice fraction	OI	Inst
OIceTck	ice water equivalent of sea ice	OI	Inst
OSnwTck	snow water equivalent over sea ice	OI	Inst
O_SSTSST	sea surface temperature	O	Inst
O_TepIce	sea ice surface temperature	I	Inst
O_CO2FLX	CO2 flux	OI	Inst

953

954 **Table A3 Fields received by CanNEMO from CanCPL. Descriptions as in Table 1.**

Field Received	Field Description	Area	Avg
O_OTaux1	Atm-ocn wind stress (x)	O	avg
O_OTauy1	Atm-ocn wind stress (y)	O	avg
O_ITaux1	Atm-ice wind stress (x)	I	avg
O_ITauy1	Atm-ice wind stress (y)	I	avg
O_QsrMix	solar heat flux mixed over ocean-ice	OI	avg
O_QsrIce	solar heat flux over sea ice	I	avg
O_QnsMix	non-solar heat flux mixed over ocean-ice	OI	avg
O_QnsIce	non-solar heat flux over sea ice	I	avg
OTotEvap	Total evaporation (evap + sublimation )	OI	avg
OIceEvap	sublimation over sea ice	I	avg
OTotSnow	Snow	C	avg



OTotRain	Rain	C	avg
O_dQnsdT	non-Solar sensitivity to temperature	I	avg
O_Runoff	runoff	OI	avg
O_Wind10	10 meter wind	C	avg
O_TauMod	ocean wind stress modulus	O	avg
O_MSLP	Mean sea level pressure	C	avg
O_AtMCO2	atm CO2 concentration	C	avg

955

956 **Table A4 Fields sent from CanAM to CanCPL. Descriptions as in Table 1.**

Field Sent	Field Description	Area	Avg
UFSO_atm	Atm-ocn wind stress (x)	O	avg
VFSO_atm	Atm-ocn wind stress (y)	O	avg
UFSI_atm	Atm-ice wind stress (x)	I	avg
VFSI_atm	Atm-ice wind stress (y)	I	avg
FSGO_atm	Solar heat flux over ocean	O	avg
FSGI_atm	Solar heat flux over ice	I	avg
BEGO_atm	Total heat flux over ocean	O	avg
BEGI_atm	Total heat flux over sea ice	I	avg
RAIN_atm	Total liquid precipitation	C	avg
SNOW_atm	Total solid precipitation	C	avg
BWGO_atm	ocean freshwater budget (P-E)	O	avg
BWGI_atm	sea ice fresh water budget	I	avg
SLIM_atm	non-Solar sensitivity to temperature	I	avg
RIVO_atm	River discharge	OI	avg
SWMX_atm	Mixed 10 meter wind	C	avg
PMSL_atm	Mean sea level pressure	C	avg
CO2_atm	Atm CO2 concentration	C	avg

957

958

959

960



961 **Appendix B: Code management and model infrastructure**

962 **Table B1: Code management**

Item	Description
Source control	Each model component and supporting tools are version controlled in a dedicated git repository. Specific component versions are tracked as submodules by the CanESM super-repo, to define a version of CanESM.
Branching structure / workflow	Development of CanESM5 code follows a <i>gitflow</i> like workflow, commonly found in industry. Each logical unit of work is first described by an <i>issue</i> . Code changes are implemented on a dedicated feature branch. For simplicity, the feature branch is created in all submodules. Upon completion and acceptance, the feature branch is merged back onto the <i>develop_canesm</i> branch, which represents the latest state of the coupled model. Periodic tags on the <i>develop_canesm</i> branch mark stable versions of the model, which are then used for production purposes. The model version used for CMIP6 production is tagged as “CanESM.v5.0.0”, and can be used to reproduce all existing CMIP6 simulations. A series of modified git commands is used to aid in working with submodules.
Versioning	Release versions of CanESM are tagged on the <i>develop_canesm</i> branch. Tags appear as CanESM.vXYZ, where X is the major version, Y is a minor number, and Z is a bugfix level number. For example, CanESM.v5.0.2. Over the course of CMIP6 development, only bit-pattern preserving changes have been accepted.
Forcing & initialization files	Forcing and initialization files are important for reproducibility, but not directly amenable to version control. An additional repository named <i>CanForce</i> contains the source code for scripts which produced the original input files. Input files are also checksummed, and a list of these checksums is tracked in the CanESM super-repository.
External dependencies	Specific versions of third party libraries, such as NetCDF, are loaded via an initialization procedure. Third party library source code is not directly tracked.

963

964

965



966 **Table B2: Process for running CanESM**

Item	Description
Run setup	Runs are setup on the ECCC HPC using a single entry point script ( <i>setup-canesm</i> ), which recursively clones the CanESM super-repository, and extracts some specific run configuration files. Hence, each run has a self-contained, full copy of the CanESM source code. This isolates runs from “external” changes, and also allows experimentation without affecting runs. When generating ensembles, code sharing between members is possible. <i>setup-canesm</i> also undertakes logging, recording which specific commit of CanESM was used in the run.
Run time environment	CanESM5 is run under Linux on ECCC’s HPC. The user environment begins as only containing the path to <i>setup-canesm</i> . A machine-specific environment setup files is extracted from CCCma_tools by this utility script, and is sourced to define the runtime environment. The runtime environment essentially re-defines the PATH variable to point to the locally extracted scripting, as well as defining a host of machine-specific environment variables required at runtime.
Compilation	<i>setup-canesm</i> extracts utility compilation scripts. Ultimately, compilation scripts call the make utility to compile the code. The compilation of CanNEMO depends on the makenemo utility included in the source. Compilation of CanAM and CanCPL is done with makefiles, which are generated by the build-exe script, which determines required dependencies.
Configuration	CanESM runs are configured via the <i>canesm.cfg</i> file, which is extracted from the CanESM super-repo by <i>setup-canesm</i> . The configuration file allows selection of type of experiment (forcing files), start and end dates, diagnostics to be undertaken, and various options like dumping files to tape and deleting files. This configuration file is automatically captured in a dedicated configuration repository for posterity.
Sequencing	A legacy set of sequencing scripting is used to run CanESM simulations. In essence, a script called <i>cccjob</i> uses the information in <i>canesm.cfg</i> to create a sequential <i>string</i> of bash scripts, which run the model, compute diagnostics, and so forth. Such <i>jobstrings</i> are submitted to the HPC scheduler, and iterated over in sequence by a series of scripts contained in the <i>CCCma_tools</i> repository.





Strict checking	“Strict checking” is implemented during compilation, configuration, and during each increment over which the model is run when in production mode for official activities like CMIP6. Strict checking ensures that any source code changes have been committed, and that any configuration changes are captured in a dedicated repository.
-----------------	--

967

968 **Appendix C: Code optimization**

969 **Table C1: Description of optimization improvements to CanESM5. See Fig. 3 for a graphical representation.**

Description of change	Throughput improvement (ypd)
Several I/O heavy operations, such as splitting and repacking files that were running in serial with the model execution were switched to run in parallel on the post-processing machine. In addition, the job submission scripting was simplified.	0.4
Splitting multi-year forcing files into yearly chunks resulted in speed improvement due to the non-sequential access of the CCCma file format.	1.1
Compiler flag optimization. Specifically the "-fp-model precise" was replaced with "-mp1" flag in the final 32-bit version, and the "-init=arrays -init=zero" flags were eliminated. The optimization level was increased from "-O1" to "-O2".	1.5
Adding a node to the CanAM component to speed up spectral transforms, and implement sharing of one node with the coupler (no increase in the overall node count).	1.2
Converting CanAM from 64 to 32 bit numerics	4.1
Writing model output from different cores/tasks into separate files (labeled in Fig. 3 as "parallel I/O"), and rebuilding them in parallel on the post-processing machine.	0.4
Changing model execution from occurring in monthly chunks (with re-initialization from restarts at the beginning of every month), to occurring in annual chunks.	2.6



970 **Appendix D: CMIP6 MIP participation and model variants**

971 **Table D1: List of MIPs and model variants of CanESM5 planned for submission to CMIP6.**

MIP	Model variant
DECK-historical	CanESM5-p1, CanESM5-p2, CanESM5-CanOE-p2
C4MIP	CanESM5-p1, CanESM5-p2
CDRMIP	CanESM5-p1, CanESM5-p2
CFMIP	CanESM5-p2
DAMIP	CanESM5-p1
DCPP	CanESM5-p2
FAFMIP	CanESM5-p2
GeoMIP	CanESM5-p2
GMMIP	CanESM5-p2
ISMIP6	CanESM5-p1, CanESM5-p2
LS3MIP	CanESM5-p1, CanESM5-p2
LUMIP	CanESM5-p1, CanESM5-p2
OMIP	CanESM5, CanESM5-CanOE (uncoupled).
PAMIP	CanESM5-p2
RFMIP	CanESM5-p2
ScenarioMIP	CanESM5-p1, CanESM5-p2, CanESM5-CanOE-p2
VolMIP	CanESM5-p2
CORDEX	N/A (CanRCM)
DynVar	CanESM5-p2
SIMIP	CanESM5-p1, CanESM5-p2

972

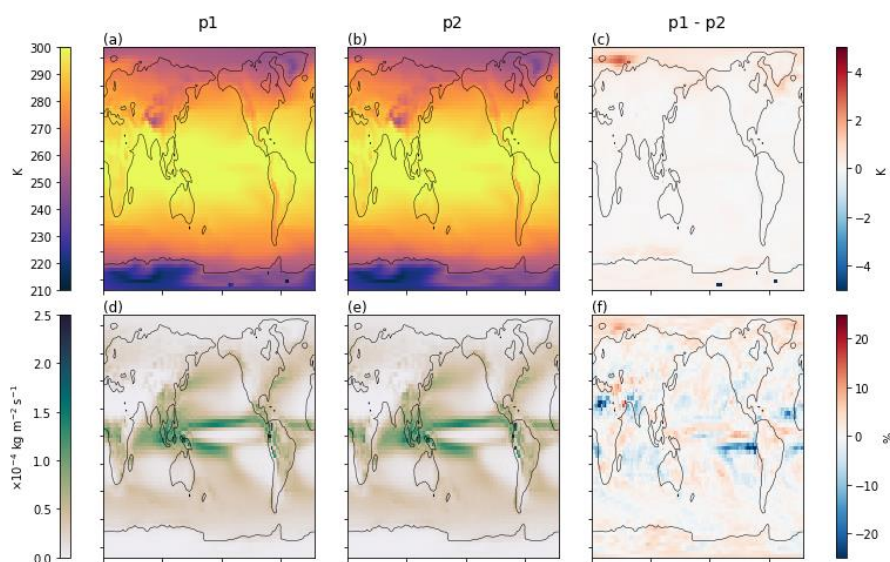


973 **Appendix E: Comparison between p1 and p2**

974 Sections 2.5 and 3.4 described the technical differences between perturbed physics members p1 and p2, submitted to the  
975 CMIP6 archive. Here we provide a preliminary analysis of the differences between the two model variants.

976

977 Fig. E1 shows surface air temperature and precipitation averaged over 200 years of piControl experiment, for p1, p2 and the  
978 difference between them. Notable in the differences are the “cold” spots in Antarctica, which arise from a mis-specified land  
979 fraction in p1, and were resolved in p2. Otherwise there are no significant differences.



980

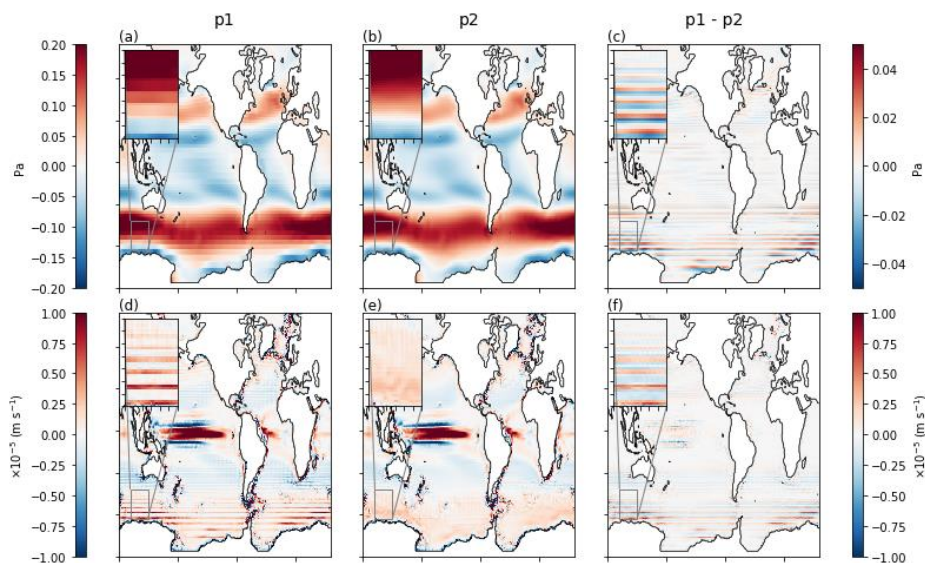
981 **Fig. E1: Climatologies of surface air temperature (a, b) and precipitation (d, e,) computed over 200 years of piControl**  
982 **simulation of the p1 (a, d) and p2 (b, e) model variants, and the differences between p1 and p2 (c, f).**

983

984 Fig E2 shows the ocean surface wind-stress. The blockiness of the field in p1 is evident, as a result of conservative remapping  
985 from CanAM. In p2, bilinear remapping was used and the field is smooth on the NEMO grid. The non-smooth nature of wind-  
986 stress in p1 resulted in, for example, banding in vertical ocean velocities at 100 m depth, as also shown in Fig. E2d. This does  
987 not occur in p2.



988



989

990

991

992

993

994

**Fig. E2:** Climatologies of surface ocean zonal wind stress (a, b) and vertical velocity near 100 m depth (d, e) computed over 200 years of piControl simulation of the p1(a, d) and p2 (b, e) model variants, and the differences between p1 and p2 (c, f). Results are shown on the native NEMO grid. The insets show an enlargement of the Southern Ocean south of Australia.

995

996

997

998

999

The response to CO<sub>2</sub> forcing in the 1pctCO<sub>2</sub> experiments in p1 and p2 is shown in Fig. E3. The global mean top of atmosphere radiation (Fig E3a) and surface air temperature (Fig E3b) responses are indistinguishable, and hence the TCR of these model variants is the same. The ocean is cooler, on average, in p2, but the perturbative response in p1 and p2 are similar (Fig E3c). Ocean surface CO<sub>2</sub> flux is also statistically indistinguishable between the variants (Fig E3d).

1000

1001

1002

1003

1004

1005

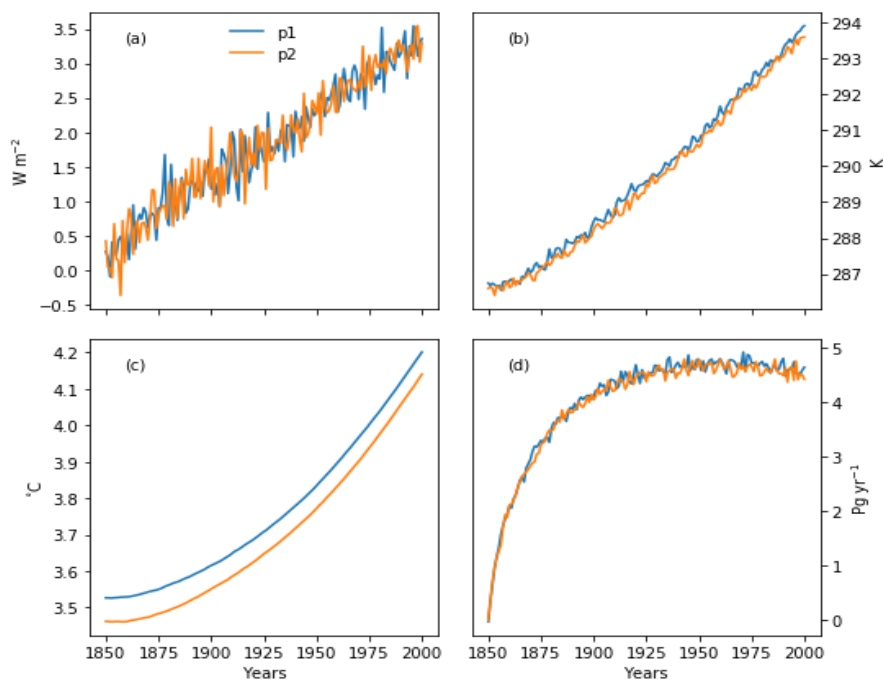
1006

1007

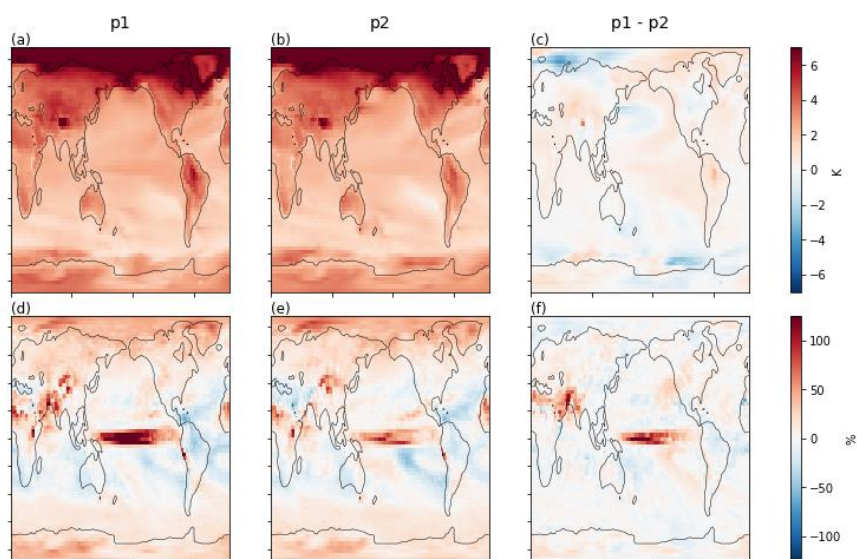
1008

1009

Maps of the perturbative response, computed as the mean over the 20 years centered on CO<sub>2</sub> doubling in the 1pctCO<sub>2</sub> experiments, minus the piControl, are shown in Figs. E4 and E5. There are no fundamental differences in the surface climate response between the two model variants.



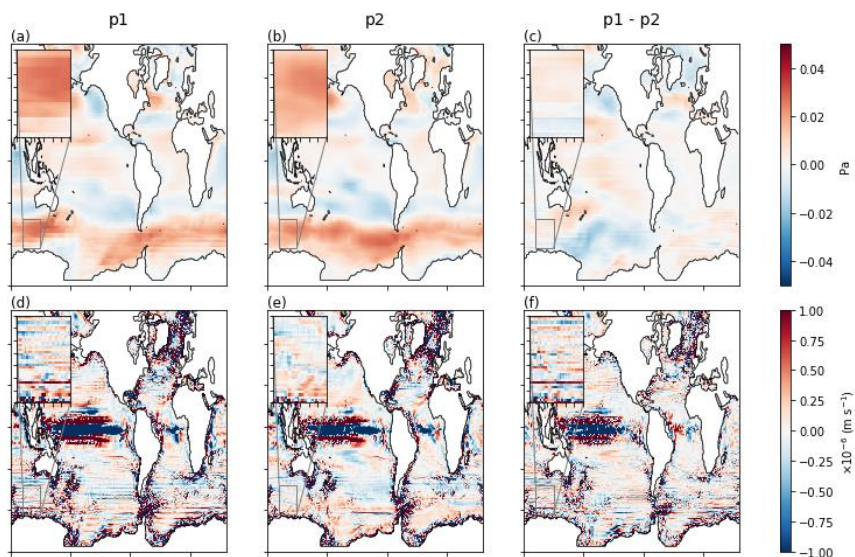
1010  
1011 **Fig. E3: Global averages of (a) top of atmosphere net radiative flux, (b) surface air temperature, (c) volume averaged**  
1012 **ocean temperature and (d) surface ocean CO<sub>2</sub> flux in the 1pctCO<sub>2</sub> simulations from the p1 and p2 model variants.**  
1013



1014  
1015 **Fig. E4: Perturbation of surface air temperature (a, b) and precipitation (d, e) computed as the mean over the 20**  
1016 **years centered on CO<sub>2</sub> doubling in the 1pctCO<sub>2</sub> experiment, minus the mean from 200 years of piControl simulation**  
1017 **of the p1 (a, d) and p2 (b, e) model variants, and the differences between p1 and p2 (c, f).**



1018



1019

1020

1021

1022

1023

1024

1025

1026

1027

1028

1029

1030

1031

1032

1033

1034

1035

**Fig. E5: Perturbations of surface ocean zonal wind stress (a, b) and vertical velocity near 100 m depth (d, e) computed as the mean over the 20 years centered on CO<sub>2</sub> doubling in the 1pctCO<sub>2</sub> experiment, minus the mean over 200 years of piControl simulation of the p1 (a, d) and p2 (b, e) model variants, and the differences between p1 and p2 (c, f). Results are shown on the native NEMO grid. The insets show an enlargement of the Southern Ocean south of Australia.**



1036 **Appendix F: Data sources, variables, and derived quantities**

1037 **Table F1: List of figures, CanESM5 CMIP6 variables, and observations used, and the time-periods of analysis.**

1038

Fig No	CMIP6 variables	CMIP6 experiment and (variant label)	Observations	Time period of analysis
4	tas	piControl, historical, abrupt-4xCO2, 1pctCO2, SSP5-85, SSP (r1i1p1f1)	n/a	1850-2100
5	rtmt, hfds, thetao, tas, wfo, zos, sivol, snw, nep, fgco2, cLand, dissic (piControl)	piControl (r1i1p1f1)	n/a	5200-6200
6	As labelled.	historical (r1i1p1f1)	ERA5, GPCP, GBAF, WOA09, AVISO, GLODAPv2.2016, ISCCP-H, AVISO MDT, NSIDC, Landschützer et al. (2015)	
7	tas, pr, psl	historical (r1i1p1f1)	ERA5, GPCP	1981-2010
8	clt	historical (r1i1p1f1)	ISCCP-H	1991-2010 (ISCCP data period)
9	ta	historical (r1i1p1f1)	ERA5	1981-2010
10	ua	historical (r1i1p1f1)	ERA5	1981-2010
11	uas	historical (r1i1p1f1)	ERA5	1981-2010
12	gpp, hfsl, and hfss	historical (r1i1p1f1)	GBAF	1982-2009 (GBAF data period)
13	gpp, hfsl, and hfss	historical (r1i1p1f1)	GBAF	1982-2009 (GBAF data period)



14	gpp, tas, pr	historical (r1i1p1f1)	GBAF	1982-2009 (GBAF data period)
15	tos, sos, zos	historical (r1i1p1f1)	WOA09, AVISO MDT	1981-2010
16	thetao, so	historical (r1i1p1f1)	WOA09	1981-2010
17	msftmz	historical (r1i1p1f1)	-	1981-2010
18	hfbasin	historical (r1i1p1f1)	Ganachaud and Wunsch (2003)	1981-2010
19	siconc, sithick	historical (r1i1p1f1 to r25i1p1f1)	NSIDC	1981-2010
20	siconc	historical (r1i1p1f1)	NSIDC	1981-2010
21	dissic, no3, o2	historical (r1i1p1f1)	GLODAPv2.2016	1981-2010
22	fgco2	historical (r1i1p1f1)	Landschützer et al. (2015)	1982-2010 (Landschützer data period)
23	tos	historical (r1i1p1f1 to r10i1p1f1)	HadISST	1850-2014
24	psl	historical (r1i1p1f1)	ERA5	1981-2010
25	tas	historical (r1i1p1f1 to r25i1p1f1)	Berkeley-Earth, HadCRUT4, NASA-GISS	Time series: 1850-2014 Trends: 1981-2014
26	tas	historical (r1i1p1f1 to r25i1p1f1)	Berkeley-Earth, HadCRUT4, NASA-GISS	1981-2014
27	siconc	historical (r1i1p1f1 to r25i1p1f1)	NSIDC	Time series: 1850-2014 Trends: 1981-2014
28	fgco2, nep, co2	historical (r1i1p1f1 to r25i1p1f1)	Le Quéré et al. (2018)	1850-2014

1039

1040

1041

1042





1043 **Table F2: List of observational products used.**

Data source	Citation
AVISO MDT	<a href="https://www.aviso.altimetry.fr/en/data/products/auxiliary-products/mdt.html">https://www.aviso.altimetry.fr/en/data/products/auxiliary-products/mdt.html</a>
ERA5	Copernicus Climate Change Service (2017)
GPCP	Adler et al. (2017)
ISCCP-H	Young et al. (2018); Rossow et al. (2016)
GBAF	Jung et al. (2009)
World Ocean Atlas 2009 (WOA09)	Locarnini et al. (2009); Antonov et al. (2010)
NSIDC sea-ice concentration	Peng et al. (2013); Meier et al. (2017)
PIOMAS	Zhang et al. (2003)
GIOMAS	Zhang et al. (2003)
GLODAPv2	Lauvset et al. (2016)
Landschützer	Landschützer et al. (2015)
HadISST	Rayner et al. (2003)
Berkley Earth	<a href="http://berkeleyearth.org/land-and-ocean-data/">http://berkeleyearth.org/land-and-ocean-data/</a>
HadCRUT4	Morice et al. (2012)
NASA-GISS	GISSTEMP Team (2019); Lenssen et al. (2019)
Global Carbon Budget 2018	Le Quéré et al. (2018)

1044

1045

1046 In Figure 28 the diagnosed allowable anthropogenic fossil fuel emissions are calculated via Equation (F1):

$$1047 \quad \frac{d[\text{CO}_2]}{dt} = E - F_L - F_O = E - (F'_L - E_{LUC}) - F_O \quad (\text{F1}).$$

1048 In these historical simulations, the concentration of atmospheric CO<sub>2</sub> is specified (that is the term d[CO<sub>2</sub>]/dt is known) and the  
 1049 model's land and ocean carbon cycle components simulate atmosphere-land (F<sub>L</sub>) and atmosphere-ocean (F<sub>O</sub>) CO<sub>2</sub> fluxes,  
 1050 respectively. The F<sub>L</sub>=F'<sub>L</sub>-E<sub>LUC</sub> term includes natural atmosphere-land CO<sub>2</sub> flux (F'<sub>L</sub>) and the emissions associated with land  
 1051 use change (E<sub>LUC</sub>) which are calculated interactively in the model in response to the historical increase in cropland area. As a  
 1052 result, the term E can be calculated and represents the allowable anthropogenic fossil fuel emissions.

1053

1054 Le Quéré et al. (2018) do not provide a direct value of net cumulative atmosphere-land CO<sub>2</sub> flux (F<sub>L</sub>). Instead, they separately  
 1055 provide estimates of cumulative values of F'<sub>L</sub> (185±50 Pg C) and E<sub>LUC</sub> (195±75) in their Table 8. Here, we calculate  
 1056 observation-based value of F<sub>L</sub>=F'<sub>L</sub>-E<sub>LUC</sub> =185-195 = -10 Pg C and its uncertainty as 90 Pg C (the uncertainty is calculated as,  
 1057  $\sqrt{(50^2 + 75^2)} = 90.13$  PgC. The large uncertainty range for the observation-based estimate of cumulative F<sub>L</sub> is therefore due  
 1058 to large uncertainties in both land use change emissions and the natural atmosphere-land CO<sub>2</sub> flux.

1059



1060 **Author contributions**

1061 NCS co-led CanESM5 development, contributed to CanNEMO and CMOC development and the data request, performed  
1062 simulations, led the creation of the figures and wrote most of the manuscript; JNSC contributed to development of CanAM5,  
1063 CanCPL and tuning of CanESM5, wrote the CanAM5 section, performed simulations and contributed to the data request; VK  
1064 contributed to the development of CanAM, notably optimization, contributed to the data request, and performed production  
1065 simulations; ML contributed to the development of CanAM, CanCPL and the data request; JS co-led CanESM5 development;  
1066 NG contributed to CanESM5 development and tuning; JA contributed to CanCPL development, the data request, and led  
1067 publication of data on the ESGF; VA contributed to the development of CLASS and CTEM; JC developed CanOE and  
1068 contributed to CMOC development; SH produced many of the figures; YJ contributed to the data request and conversion; WL  
1069 contributed to CanNEMO development and ran simulations; FM contributed to the CanESM5 software infrastructure; OS led  
1070 ocean physics testing; provided a specific analysis that motivated the p2 variant; ChS contributed analysis of the land  
1071 component; CIS contributed to CanESM5 software infrastructure; AS created Fig. 23, contributed to CanESM5 development,  
1072 and performed simulations; LS developed CanCPL; KVS led the development and tuning of atmospheric model  
1073 parameterizations; DY contributed to ocean model development, ocean and sea ice diagnostics for CMIP6, and performed  
1074 production simulations; BW processed forcing datasets for CanAM; All authors contributed to editing the manuscript.

1075 **Competing interests**

1076 No competing interests.

1077 **Disclaimer**

1078 CanESM has been customized to run on the ECCC high performance computer, and a significant fraction of the software  
1079 infrastructure used to run the model is specific to the individual machines and architecture. While we publicly provide the  
1080 code, we cannot provide any support for migrating the model to different machines or architectures.

1081 **Special issue statement (will be included by Copernicus)**

1082 To be included in the CanESM5 special issue.

1083 **Acknowledgements**

1084 We acknowledge Dr. Michael Sigmond, Dr. Greg Flato and Dr. William Merryfield for helpful comments on a draft of the  
1085 paper. CanESM5 was the cumulative result of work by many individuals, who we thank for their contributions. CanESM5  
1086 simulations were performed on ECCC's HPC, and CanESM5 data is served via the Earth System Grid Federation.



1087 **References**

- 1088 Adler RF, Sapiano M, Huffman GJ, et al.: The Global Precipitation Climatology Project (GPCP) Monthly Analysis (New  
1089 Version 2.3) and a Review of 2017 Global Precipitation. *Atmosphere* (Basel), 2018;9(4):138. doi:10.3390/atmos9040138,  
1090 2018.
- 1091
- 1092 Antonov, J. I., Seidov, D., Boyer, T. P., Locarnini, R. A., Mishonov, A. V., Garcia, H. E., Baranova, O. K., Zweng, M. M.,  
1093 and Johnson, D. R.: *World Ocean Atlas 2009, Volume 2: Salinity*. S. Levitus, Ed. NOAA Atlas NESDIS 69, U.S.  
1094 Government Printing Office, Washington, D.C., 184 pp, 2010.
- 1095
- 1096 Arora, V.K.: Simulating energy and carbon fluxes over winter wheat using coupled land surface and terrestrial ecosystem  
1097 models. *Agricultural and Forest Meteorology*. 118(1-2), 21-47, 2003.
- 1098
- 1099 Arora, V.K., and Boer, G.J.: A variable velocity flow routing algorithm for GCMs, *J. Geophys. Res.*, 104, D24, 30965-  
1100 30979, 1999.
- 1101
- 1102 Arora, V.K. and Boer, G.J.: A representation of variable root distribution in dynamic vegetation models. *Earth Interactions*.  
1103 Vol. 7, Paper 6, 19 pp, 2003.
- 1104
- 1105 Arora, V.K. and Boer, G.J.: A parameterization of leaf phenology for the terrestrial ecosystem component of climate models.  
1106 *Global Change Biology*. 11(1), 39-59, 2005.
- 1107
- 1108 Arora, V. K., Boer, G. J., Christian, J. R., Curry, C. L., Denman, K. L., Zahariev, K., Flato, G. M., Scinocca, J. F.,  
1109 Merryfield, W. J. and Lee, W. G.: The effect of terrestrial photosynthesis down-regulation on the 20th century carbon budget  
1110 simulated with the CCCma Earth System Model. *J. Clim.* 22, 6066-6088, 2009.
- 1111
- 1112 Arora, V.K. and Boer, G.J.: Uncertainties in the 20th century carbon budget associated with land use change. *Global Change*  
1113 *Biology*. 16(12), 3327-3348, 2010.
- 1114
- 1115 Arora, V. K., Scinocca, J. F., Boer, G. J., Christian, J. R., Denman, K. L., Flato, G. M., Kharin, V. V., Lee, W. G., and  
1116 Merryfield, W. J.: Carbon emission limits required to satisfy future representative concentration pathways of greenhouse  
1117 gases, *Geophys. Res. Lett.*, 38, L05805, doi:[10.1029/2010GL046270](https://doi.org/10.1029/2010GL046270), 2011.
- 1118



- 1119 Arora, V. K. and Scinocca, J. F.: Constraining the strength of the terrestrial CO<sub>2</sub> fertilization effect in the Canadian Earth  
1120 system model version 4.2 (CanESM4.2), *Geosci. Model Dev.*, 9, 2357-2376, <https://doi.org/10.5194/gmd-9-2357-2016>,  
1121 2016.  
1122
- 1123 Arora, V. K., Melton, J. R., and Plummer, D.: An assessment of natural methane fluxes simulated by the CLASS-CTEM  
1124 model, *Biogeosciences*, 15, 4683-4709, <https://doi.org/10.5194/bg-15-4683-2018>, 2018.  
1125
- 1126 Bartholomé, E. and Belward, A. S.: GLC2000: a new approach to global land cover mapping from Earth observation data,  
1127 *International Journal of Remote Sensing*, 26:9, 1959-1977, DOI: [10.1080/01431160412331291297](https://doi.org/10.1080/01431160412331291297), 2005.  
1128
- 1129 Bentsen, M., Bethke, I., Debernard, J. B., Iversen, T., Kirkevåg, A., Seland, Ø., Drange, H., Roelandt, C., Seierstad, I. A.,  
1130 Hoose, C., and Kristjánsson, J. E.: The Norwegian Earth System Model, NorESM1-M – Part 1: Description and basic  
1131 evaluation of the physical climate, *Geosci. Model Dev.*, 6, 687-720, <https://doi.org/10.5194/gmd-6-687-2013>, 2013.  
1132
- 1133 Boer, G. J., and McFarlane, N. A.: The AES atmospheric general circulation model. Report of the JOC Study Conference on  
1134 Climate Models: Performance, Intercomparison and Sensitivity Studies, Vol. I, GARP Publ. Ser. No. 22, pp. 409–460, 1979.  
1135
- 1136 Boer, G. J., McFarlane, N. A., Laprise, R., Henderson, J. D., and Blanchet, J.-P.: The Canadian Climate Centre Spectral  
1137 Atmospheric General Circulation Model, *Atmos.–Ocean*, 22(4), 397–429, 1984.  
1138
- 1139 Boer, G.J., Flato, G.M., Reader, M.C., and Ramsden, D.: A transient climate change simulation with historical and projected  
1140 greenhouse gas and aerosol forcing: experimental design and comparison with the instrumental record for the 20th century.  
1141 *Climate Dynamics*, 16, 405-425, 2000a.  
1142
- 1143 Boer, G.J., Flato, G.M, and Ramsden, D.: A transient climate change simulation with historical and projected greenhouse gas  
1144 and aerosol forcing: projected climate for the 21st century. *Climate Dynamics*, 16, 427-450, 2000b.  
1145
- 1146 Bouillon, S., Morales Maqueda, M.A., Legat, V., and Fichet, T.: An elastic-viscous-plastic sea ice model formulated on  
1147 Arakawa B and C grids. *Ocean Modelling*, 27, 174-184, doi : 10.1016/j.ocemod.2009.01.004, 2009.  
1148
- 1149 Cole et al.: The Canadian Atmospheric Model version 5. GMD special issue on CanESM5, in preparation, 2019.  
1150



- 1151 Copernicus Climate Change Service (C3S) (2017): ERA5: Fifth generation of ECMWF atmospheric reanalyses of the global  
1152 climate. Copernicus Climate Change Service Climate Data Store (CDS), 2019/05/15.  
1153 <https://cds.climate.copernicus.eu/cdsapp#!/home>  
1154
- 1155 Chelton, D. B., Schlax, M. G., and Samelson, R. M.: Global observations of nonlinear mesoscale eddies. *Prog. Oceanogr.*,  
1156 91, 167–216, <https://doi.org/10.1016/j.pocean.2011.01.002>, 2011.  
1157
- 1158 Christian, J. R., et al.: The global carbon cycle in the Canadian Earth system model (CanESM1): Preindustrial control  
1159 simulation, *J. Geophys. Res.*, 115, G03014, doi:[10.1029/2008JG000920](https://doi.org/10.1029/2008JG000920), 2010.  
1160
- 1161 Christian, J.R. et al: The Canadian Ocean Ecosystem, GMD special issue on CanESM5, in preparation, 2019.  
1162
- 1163 Collins, N., Theurich, G., DeLuca, C., Suarez, M., Trayanov, A., Balaji, V., Li, P., Yang, W., Hill, C., and da Silva, A.:  
1164 Design and Implementation of Components in the Earth System Modeling Framework. *International Journal of High*  
1165 *Performance Computing Applications*, Vol. 19, No. 3, pp. 341-350, 2005.  
1166
- 1167 Collins, M., Knutti, R., Arblaster, J., Dufresne, J.-L., Fichefet, T., Friedlingstein, P., Gao, X., Gutowski, W.J., Johns, T.,  
1168 Krinner, G., Shongwe, M., Tebaldi, C., Weaver, A.J. and Wehner, M.: Long-term Climate Change: Projections,  
1169 Commitments and Irreversibility. In: *Climate Change 2013: The Physical Science Basis. Contribution of Working Group I to*  
1170 *the Fifth Assessment Report of the Intergovernmental Panel on Climate Change* [Stocker, T.F., D. Qin, G.-K. Plattner, M.  
1171 Tignor, S.K. Allen, J. Boschung, A. Nauels, Y. Xia, V. Bex and P.M. Midgley (eds.)]. Cambridge University Press,  
1172 Cambridge, United Kingdom and New York, NY, USA, 2013.  
1173
- 1174 Donohue K.A, Tracey K.L, Watts D.R, Chidichimo M.P, Chereskin TK: Mean Antarctic Circumpolar Current transport  
1175 measured in Drake Passage, *Geophysical Research Letters*, 43, 11,760-11,767, 2016.  
1176
- 1177 ESMF Joint Specification Team: ESMF Reference Manual for Fortran.  
1178 [http://www.earthsystemmodeling.org/esmf\\_releases/public/last/ESMF\\_refdoc/ESMF\\_refdoc.html](http://www.earthsystemmodeling.org/esmf_releases/public/last/ESMF_refdoc/ESMF_refdoc.html), 2018.  
1179
- 1180 Eyring, V., Bony, S., Meehl, G. A., Senior, C. A., Stevens, B., Stouffer, R. J., and Taylor, K. E.: Overview of the Coupled  
1181 Model Intercomparison Project Phase 6 (CMIP6) experimental design and organization, *Geosci. Model Dev.*, 9, 1937-1958,  
1182 <https://doi.org/10.5194/gmd-9-1937-2016>, 2016.  
1183



- 1184 Fichet, T., and Morales Maqueda, M.A.: Sensitivity of a global sea ice model to the treatment of ice thermodynamics and  
1185 dynamics. *Journal Geophys. Res.*, 102, 12609-12646, <https://doi.org/10.1029/97JC00480>, 1997.
- 1186
- 1187 Flato, G.M., Boer, G.J., Lee, W.G., McFarlane, N.A., Ramsden, D., Reader, M.C., and Weaver, A.J.: The Canadian Centre  
1188 for Climate Modelling and Analysis Global Coupled Model and its Climate. *Climate Dynamics*, 16, 451-467, 2000.
- 1189
- 1190 Flato, G., Marotzke, J., Abiodun, B., Braconnot, P., Chou, S.C., Collins, W., Cox, P., Driouech, F., Emori, S., Eyring, V.,  
1191 Forest, C., Gleckler, P., Guilyardi, E., Jakob, C., Kattsov, V., Reason, C. and Rummukainen, M.: Evaluation of Climate  
1192 Models. In: *Climate Change 2013: The Physical Science Basis. Contribution of Working Group I to the Fifth Assessment*  
1193 *Report of the Intergovernmental Panel on Climate Change* [Stocker, T.F., D. Qin, G.-K. Plattner, M. Tignor, S.K. Allen, J.  
1194 Boschung, A. Nauels, Y. Xia, V. Bex and P.M. Midgley (eds.)]. Cambridge University Press, Cambridge, United Kingdom  
1195 and New York, NY, USA, 2013.
- 1196
- 1197 Forster, P. M., Richardson, T., Maycock, A. C., Smith, C. J., Samset, B. H., Myhre, G., Andrews, T., Pincus, R., and Schulz,  
1198 M.: Recommendations for diagnosing effective radiative forcing from climate models for CMIP6, *J. Geophys. Res. Atmos.*,  
1199 121, 12,460– 12,475, doi:10.1002/2016JD025320, 2016.
- 1200
- 1201 Ganachaud, A. and Wunsch, C.: Large-Scale Ocean Heat and Freshwater Transports during the World Ocean Circulation  
1202 Experiment. *J. Climate*, 16, 696–705, [https://doi.org/10.1175/1520-0442\(2003\)016<0696:LSOHAF>2.0.CO;2](https://doi.org/10.1175/1520-0442(2003)016<0696:LSOHAF>2.0.CO;2), 2003.
- 1203
- 1204 Gaspar, P., Grégoris, Y., and Lefevre, J.-M.: A simple eddy kinetic energy model for simulations of the oceanic vertical  
1205 mixing: Tests at station Papa and long-term upper ocean study site. *J. Geophys. Res.*, 95, 16179–16193,  
1206 <https://doi.org/10.1029/JC095iC09p16179>, 1990.
- 1207
- 1208 Gent, P. R., and McWilliams, J. C.: Isopycnal mixing in ocean general circulation models. *J. Phys. Oceanogr.*, 20, 150–155,  
1209 [https://doi.org/10.1175/1520-0485\(1990\)020<0150:IMIOCM.2.0.CO;2](https://doi.org/10.1175/1520-0485(1990)020<0150:IMIOCM.2.0.CO;2), 1990.
- 1210
- 1211 Gillett, N.P., Arora, V.K., Matthews, D., and Allen, M.R.: Constraining the Ratio of Global Warming to Cumulative CO<sub>2</sub>  
1212 Emissions Using CMIP5 Simulations. *J. Climate*, 26, 6844–6858, <https://doi.org/10.1175/JCLI-D-12-00476.1>, 2013.
- 1213
- 1214 GISTEMP Team: GISS Surface Temperature Analysis (GISTEMP), version 4. NASA Goddard Institute for Space Studies.  
1215 Dataset accessed 2019-04-07 at <https://data.giss.nasa.gov/gistemp/>, 2019.
- 1216



- 1217 Gregory, J. M., Ingram, W. J., Palmer, M. A., Jones, G. S., Stott, P. A., Thorpe, R. B., Lowe, J. A., Johns, T. C., and  
1218 Williams, K. D.: A new method for diagnosing radiative forcing and climate sensitivity, *Geophys. Res. Lett.*, 31, L03205,  
1219 doi:[10.1029/2003GL018747](https://doi.org/10.1029/2003GL018747), 2004.
- 1220
- 1221 Hewitt, H. T., Copsey, D., Culverwell, I. D., Harris, C. M., Hill, R. S. R., Keen, A. B., McLaren, A. J., and Hunke, E. C.:  
1222 Design and implementation of the infrastructure of HadGEM3: the next-generation Met Office climate modelling system,  
1223 *Geosci. Model Dev.*, 4, 223-253, <https://doi.org/10.5194/gmd-4-223-2011>, 2011.
- 1224
- 1225 Hill, C., DeLuca, C., Balaji, V., Suarez, M., and da Silva, A.: Architecture of the Earth System Modeling Framework.  
1226 *Computing in Science and Engineering*, Vol. 6, No. 1, pp. 18-28, 2004.
- 1227
- 1228 Hurtt, G.C., Chini, L. P., Frolking, S., Betts, R. A., Feddema, J., Fischer, G., Fisk, J. P., Hibbard, K., Houghton, R. A.,  
1229 Janetos, A., Jones, C. D., Kindermann, G., Kinoshita, T., Goldewijk, K.K., Riahi, K., Shevliakova, E., Smith, S., Stehfest, E.,  
1230 Thomson, A., Thornton, P., van Vuuren, D. P. and Wang, Y. P.: Harmonization of land-use scenarios for the period 1500–  
1231 2100: 600 years of global gridded annual land-use transitions, wood harvest, and resulting secondary lands. *Climatic Change*  
1232 109:117–161 DOI 10.1007/s10584-011-0153-2, 2011.
- 1233
- 1234 IPCC: Climate Change 2013: The Physical Science Basis. Contribution of Working Group I to the Fifth Assessment Report  
1235 of the Intergovernmental Panel on Climate Change [Stocker, T.F., Qin, D., Plattner, G.-K., Tignor, M., Allen, S.K.,  
1236 Boschung, J., Nauels, A., Xia, Y., Bex, V. and Midgley, P.M. (eds.)]. Cambridge University Press, Cambridge, United  
1237 Kingdom and New York, NY, USA, 1535 pp, doi:10.1017/CBO9781107415324, 2013.
- 1238
- 1239 Jung, M., Reichstein, M., and Bondeau, A.: “Towards Global Empirical Upscaling of FLUXNET Eddy Covariance  
1240 Observations: Validation of a Model Tree Ensemble Approach Using a Biosphere Model.” *Biogeosciences* 6 (10): 2001–13.,  
1241 2009
- 1242
- 1243 Kay, J.E., Deser, C., Phillips, A., Mai, A., Hannay, C., Strand, G., Arblaster, J.M., Bates, S.C., Danabasoglu, G., Edwards, J.,  
1244 Holland, M., Kushner, P., Lamarque, J., Lawrence, D., Lindsay, K., Middleton, A., Munoz, E., Neale, R., Oleson, K.,  
1245 Polvani, L., and Vertenstein, M.: The Community Earth System Model (CESM) Large Ensemble Project: A Community  
1246 Resource for Studying Climate Change in the Presence of Internal Climate Variability. *Bull. Amer. Meteor. Soc.*, 96, 1333–  
1247 1349, <https://doi.org/10.1175/BAMS-D-13-00255.1>, 2015.
- 1248
- 1249 Kirchmeier-Young, M.C., Zwiers, F.W., and Gillett, N.P.: [Attribution of Extreme Events in Arctic Sea Ice Extent](https://doi.org/10.1175/JCLI-D-16-0412.1). *J.*  
1250 *Climate*, 30, 553–571, <https://doi.org/10.1175/JCLI-D-16-0412.1>, 2017.



- 1251
- 1252 Landschützer, P., Gruber, N. and Bakker, D.C.E.: A 30 year observation-based global monthly gridded sea surface pCO<sub>2</sub>
- 1253 product from 1982 through 2011 [http://cdiac.ornl.gov/ftp/oceans/spco2\\_1982\\_2011\\_ETH\\_SOM-FFN](http://cdiac.ornl.gov/ftp/oceans/spco2_1982_2011_ETH_SOM-FFN). Carbon Dioxide
- 1254 Information Analysis Center, Oak Ridge National Laboratory, US Department of Energy, Oak Ridge, Tennessee. doi:
- 1255 10.3334/CDIAC/OTG.SPCO2\_1982\_2011\_ETH\_SOM-FFN, 2015.
- 1256
- 1257 Lauvset, S. K., Key, R. M., Olsen, A., van Heuven, S., Velo, A., Lin, X., Schirnick, C., Kozyr, A., Tanhua, T., Hoppema,
- 1258 M., Jutterström, S., Steinfeldt, R., Jeansson, E., Ishii, M., Perez, F. F., Suzuki, T., and Watelet, S.: A new global interior
- 1259 ocean mapped climatology: the 1° × 1° GLODAP version 2, *Earth Syst. Sci. Data*, 8, 325-340, [https://doi.org/10.5194/essd-](https://doi.org/10.5194/essd-8-325-2016)
- 1260 8-325-2016, 2016.
- 1261
- 1262 Le Quéré, C., Andrew, R. M., Friedlingstein, P., Sitch, S., Hauck, J., Pongratz, J., Pickers, P. A., Korsbakken, J. I., Peters, G.
- 1263 P., Canadell, J. G., Arneeth, A., Arora, V. K., Barbero, L., Bastos, A., Bopp, L., Chevallier, F., Chini, L. P., Ciais, P., Doney,
- 1264 S. C., Gkritzalis, T., Goll, D. S., Harris, I., Haverd, V., Hoffman, F. M., Hoppema, M., Houghton, R. A., Hurtt, G., Ilyina, T.,
- 1265 Jain, A. K., Johannessen, T., Jones, C. D., Kato, E., Keeling, R. F., Goldewijk, K. K., Landschützer, P., Lefèvre, N., Lienert,
- 1266 S., Liu, Z., Lombardozi, D., Metzl, N., Munro, D. R., Nabel, J. E. M. S., Nakaoka, S.-I., Neill, C., Olsen, A., Ono, T., Patra,
- 1267 P., Peregón, A., Peters, W., Peylin, P., Pfeil, B., Pierrot, D., Poulter, B., Rehder, G., Resplandy, L., Robertson, E., Rocher,
- 1268 M., Rödenbeck, C., Schuster, U., Schwinger, J., Séférian, R., Skjelvan, I., Steinhoff, T., Sutton, A., Tans, P. P., Tian, H.,
- 1269 Tilbrook, B., Tubiello, F. N., van der Laan-Luijkx, I. T., van der Werf, G. R., Viovy, N., Walker, A. P., Wiltshire, A. J.,
- 1270 Wright, R., Zaehle, S., and Zheng, B.: Global Carbon Budget 2018, *Earth Syst. Sci. Data*, 10, 2141-2194,
- 1271 <https://doi.org/10.5194/essd-10-2141-2018>, 2018.
- 1272
- 1273 Lenssen, N., Schmidt, G., Hansen, J., Menne, M., Persin, A., Ruedy, R., and Zyss, D.: [Improvements in the uncertainty](#)
- 1274 [model in the Goddard Institute for Space Studies Surface Temperature \(GISTEMP\) analysis](#). *J. Geophys. Res. Atmos.*, in
- 1275 press, doi:10.1029/2018JD029522, 2019.
- 1276
- 1277 Locarnini, R. A., Mishonov, A. V., Antonov, J. I., Boyer, T. P., Garcia, H. E., Baranova, O. K., Zweng, M. M., and Johnson,
- 1278 D. R.. World Ocean Atlas 2009, Volume 1: Temperature. S. Levitus, Ed. NOAA Atlas NESDIS 68, U.S. Government
- 1279 Printing Office, Washington, D.C., 184 pp, 2010.
- 1280
- 1281 Matthews, H.D., Gillett, N.P., Stott, P.A. and Zickfeld, K.. The proportionality of global warming to cumulative carbon
- 1282 emissions. *Nature* 459 (7248), 829-832, 2009.
- 1283





- 1284 Madec, G., and Coauthors: NEMO ocean engine, version 3.4. Institut Pierre-Simon Laplace Note du Pole de Modélisation  
1285 27, 367 pp., 2012.
- 1286
- 1287 Marshall, D., and Naveira Garabato, A.: A conjecture on the role of bottom-enhanced diapycnal mixing in the  
1288 parameterization of geostrophic eddies. *J. Phys. Oceanogr.*, 38, 1607–1613, 2008.
- 1289
- 1290 McCarthy, G.D., Smeed, D.A., Johns, W.E., Frajka-Williams, E., Moat, B.I., Rayner, D., Baringer, M.O., Meinen, C.S.,  
1291 Collins, J. and Bryden, H.L.: Measuring the Atlantic Meridional Overturning Circulation at 26°N, *Progress in*  
1292 *Oceanography*, Vol. 130, 91-111, <https://doi.org/10.1016/j.pocean.2014.10.006>, 2015.
- 1293
- 1294 McFarlane, N.A., Boer, G.J., Blanchet, J.-P., and Lazare, M.: The Canadian Climate Centre Second-Generation General  
1295 Circulation Model and Its Equilibrium Climate. *J. of Climate*, 5, 1013-1044, 1992.
- 1296
- 1297 Meier, W. N., Fetterer, F., Savoie, M., Mallory, S., Duerr, R., and Stroeve, J.: NOAA/NSIDC Climate Data Record of  
1298 Passive Microwave Sea Ice Concentration, Version 3. Boulder, Colorado USA. NSIDC: National Snow and Ice Data Center.  
1299 doi: <https://doi.org/10.7265/N59P2ZTG>. Last accessed 2019/04/17, 2017.
- 1300
- 1301 Merryfield, W. J., Holloway, G., and Gargett, A.E.: A global ocean model with double-diffusive mixing, *J. Phys. Ocean.*, 29,  
1302 1124–1142, 1999.
- 1303
- 1304 Merryfield, W.J., Lee, W., Boer, G.J., Kharin, V.V., Scinocca, J.F., Flato, G.M., Ajayamohan, R.S., Fyfe, J.C., Tang, Y., and  
1305 Polavarapu, S.: The Canadian Seasonal to Interannual Prediction System. Part I: Models and Initialization. *Mon. Wea. Rev.*,  
1306 141, 2910–2945, <https://doi.org/10.1175/MWR-D-12-00216.1>, 2013.
- 1307
- 1308 Morice, C.P., Kennedy, J.J., Rayner, N.A. and Jones, P.D.: Quantifying uncertainties in global and regional temperature  
1309 change using an ensemble of observational estimates: the HadCRUT4 dataset. *Journal of Geophysical Research*, 117,  
1310 D08101, [doi:10.1029/2011JD017187](https://doi.org/10.1029/2011JD017187), 2012.
- 1311
- 1312 Orr, J. C., Najjar, R. G., Aumont, O., Bopp, L., Bullister, J. L., Danabasoglu, G., Doney, S. C., Dunne, J. P., Dutay, J.-C.,  
1313 Graven, H., Griffies, S. M., John, J. G., Joos, F., Levin, I., Lindsay, K., Matear, R. J., McKinley, G. A., Mouchet, A.,  
1314 Oeschies, A., Romanou, A., Schlitzer, R., Tagliabue, A., Tanhua, T., and Yool, A.: Biogeochemical protocols and  
1315 diagnostics for the CMIP6 Ocean Model Intercomparison Project (OMIP), *Geosci. Model Dev.*, 10, 2169-2199,  
1316 <https://doi.org/10.5194/gmd-10-2169-2017>, 2017.



- 1317 Peng, G., Meier, W. N., Scott, D., and Savoie, M.: A long-term and reproducible passive microwave sea ice concentration  
1318 data record for climate studies and monitoring, *Earth Syst. Sci. Data*. 5. 311-318. <https://doi.org/10.5194/essd-5-311-2013>,  
1319 2013.
- 1320
- 1321 Rayner, N. A.; Parker, D. E.; Horton, E. B.; Folland, C. K.; Alexander, L. V.; Rowell, D. P.; Kent, E. C.; Kaplan, A.: Global  
1322 analyses of sea surface temperature, sea ice, and night marine air temperature since the late nineteenth century *J. Geophys.*  
1323 *Res.* Vol. 108, No. D14, 4407 10.1029/2002JD002670, 2003.
- 1324
- 1325 Redi, M. H.: Oceanic isopycnal mixing by coordinate rotation. *J. Phys. Oceanogr.*, 12, 1154–1158,  
1326 [https://doi.org/10.1175/1520-0485\(1982\)012,1154:OIMBCR.2.0.CO;2](https://doi.org/10.1175/1520-0485(1982)012,1154:OIMBCR.2.0.CO;2), 1982.
- 1327
- 1328 Rosenblum, E. and Eisenman, I.: Sea Ice Trends in Climate Models Only Accurate in Runs with Biased Global Warming. *J.*  
1329 *Climate*, 30, 6265–6278, <https://doi.org/10.1175/JCLI-D-16-0455.1>, 2017.
- 1330
- 1331 Rossow, W.B.; Walker, A.; Golea, V.; Knapp, K. R.; Young, A.; Inamdar A.; Hankins, B.; and NOAA's Climate Data  
1332 Record Program: International Satellite Cloud Climatology Project Climate Data Record, H-Series v1.00 NOAA National  
1333 Centers for Environmental Information. 10 May 2019. doi:10.7289/V5QZ281S, 2016.
- 1334
- 1335 Saenko, O.A., Zhai, X., Merryfield, W., and Lee, W.: The combined effect of tidally and eddy-driven diapycnal mixing on  
1336 the large-scale ocean circulation. *J. Phys. Oceanogr.*, 42, 526–538, <https://doi.org/10.1175/JPO-D-11-0122.1>, 2012.
- 1337
- 1338 Saenko, O.A., Yang, D., and Gregory, J.M.: Impact of mesoscale eddy transfer on heat uptake in an eddy-parameterizing  
1339 ocean model. *J. Climate.*, 31, 8589-8606, <https://doi.org/10.1175/JCLI-D-18-0186.1>, 2018.
- 1340
- 1341 Swart, N.C., Gille, S.T., Fyfe, J.C. and Gillett, N.P.: Recent Southern Ocean warming and freshening driven by greenhouse  
1342 gas emissions and ozone depletion. *Nature Geoscience*, 11, 836-841, 2018.
- 1343
- 1344 von Salzen, K., Scinocca, J. F., McFarlane, N. A., Li, J., Cole, J. N. S., Plummer, D., Verseghy, D., Reader, M. C., Ma, X.,  
1345 Lazare, M. and Solheim, L.: The Canadian Fourth Generation Atmospheric Global Climate Model (CanAM4). Part I:  
1346 Representation of Physical Processes, *Atmosphere-Ocean*, 51:1, 104-125, DOI: [10.1080/07055900.2012.755610](https://doi.org/10.1080/07055900.2012.755610), 2013.
- 1347
- 1348 Schurer, A., Hegerl, G., Ribes, A., Polson, D., Morice, C., and Tett, S.: Estimating the Transient Climate Response from  
1349 Observed Warming. *J. Climate*, 31, 8645–8663, <https://doi.org/10.1175/JCLI-D-17-0717.1>, 2018.



- 1350
- 1351 Scinocca, J. F., McFarlane, N. A., Lazare, M., Li, J., and Plummer, D.: Technical Note: The CCCma third generation AGCM  
1352 and its extension into the middle atmosphere, *Atmos. Chem. Phys.*, 8, 7055-7074, <https://doi.org/10.5194/acp-8-7055-2008>,  
1353 2008.
- 1354
- 1355 Scinocca, J.F., Kharin, V.V., Jiao, Y., Qian, M.W., Lazare, M., Solheim, L., Flato, G.M., Biner, S., Desgagne, M., and  
1356 Dugas, B.: Coordinated Global and Regional Climate Modeling. *J. Climate*, 29, 17–35, [https://doi.org/10.1175/JCLI-D-15-](https://doi.org/10.1175/JCLI-D-15-0161.1)  
1357 [0161.1](https://doi.org/10.1175/JCLI-D-15-0161.1), 2016.
- 1358
- 1359 Sheen, K., and Coauthors: Eddy-induced variability in Southern Ocean abyssal mixing on climatic timescales. *Nat. Geosci.*,  
1360 7, 577–582, doi:<https://doi.org/10.1038/ngeo2200>, 2014.
- 1361
- 1362 Simmons, H. L., Jayne, S. R., St. Laurent, L. C., and Weaver, A. J.: Tidally driven mixing in a numerical model of the ocean  
1363 general circulation. *Ocean Modell.*, 6, 245–263, [https://doi.org/10.1016/S1463-5003\(03\)00011-8](https://doi.org/10.1016/S1463-5003(03)00011-8), 2004.
- 1364
- 1365 Theurich, G., DeLuca, C., Campbell, T., Liu, F., Saint, K., Vertenstein, M., Chen, J., Oehmke, R., Doyle, J., Whitcomb, T.,  
1366 Wallcraft, A., Iredell, M., Black, T., Da Silva, A. M., Clune, T., Ferraro, R., Li, P., Kelley, M., Aleinov, I., Balaji, V., Zadeh,  
1367 N., Jacob, R., Kirtman, B., Giraldo, F., McCarren, D., Sandgathe, S., Peckham, S., and Dunlap IV, R.: The Earth System  
1368 Prediction Suite: Toward a Coordinated U.S. Modeling Capability. *Bulletin of the American Meteorological Society*, Vol.  
1369 97, No. 7, pp. 1229-1247, 2016.
- 1370
- 1371 UNFCCC: Paris Agreement. [https://unfccc.int/sites/default/files/english\\_paris\\_agreement.pdf](https://unfccc.int/sites/default/files/english_paris_agreement.pdf), last access 10 May 2019,  
1372 2015.
- 1373
- 1374 Versegny, D. L.: Class—A Canadian land surface scheme for GCMS. I. Soil model. *Int. J. Climatol.*, 11: 111-133.  
1375 doi:[10.1002/joc.3370110202](https://doi.org/10.1002/joc.3370110202), 1991.
- 1376
- 1377 Versegny, D. L., McFarlane, N. A. and Lazare, M.: Class—A Canadian land surface scheme for GCMS, II. Vegetation  
1378 model and coupled runs. *Int. J. Climatol.*, 13: 347-370. doi:[10.1002/joc.3370130402](https://doi.org/10.1002/joc.3370130402), 1993.
- 1379
- 1380 Versegny, D.L.: The Canadian land surface scheme (CLASS): Its history and future, *Atmosphere-Ocean*, 38:1, 1-13, DOI:  
1381 [10.1080/07055900.2000.9649637](https://doi.org/10.1080/07055900.2000.9649637), 2000.
- 1382



- 1383 West, A. E., McLaren, A. J., Hewitt, H. T., and Best, M. J.: The location of the thermodynamic atmosphere–ice interface in  
1384 fully coupled models – a case study using JULES and CICE, *Geosci. Model Dev.*, 9, 1125-1141,  
1385 <https://doi.org/10.5194/gmd-9-1125-2016>, 2016.
- 1386
- 1387 Winton, M.: Do Climate Models Underestimate the Sensitivity of Northern Hemisphere Sea Ice Cover?. *J. Climate*, 24,  
1388 3924–3934, <https://doi.org/10.1175/2011JCLI4146.1>, 2011.
- 1389
- 1390 Yang, D. and Saenko, O.A.: Ocean Heat Transport and Its Projected Change in CanESM2. *J. Climate*, 25, 8148–8163,  
1391 <https://doi.org/10.1175/JCLI-D-11-00715.1>, 2012.
- 1392
- 1393 Young, A. H., Knapp, K. R., Inamdar, A., Hankins, W., and Rossow, W. B.: The International Satellite Cloud Climatology  
1394 Project H-Series climate data record product, *Earth Syst. Sci. Data*, 10, 583-593, <https://doi.org/10.5194/essd-10-583-2018>,  
1395 2018.
- 1396
- 1397 Zahariev, K., Christian, J. R. and Denman, K. L.: Preindustrial, historical, and fertilization simulations using a global ocean  
1398 carbon model with new parameterizations of iron limitation, calcification, and N<sub>2</sub> fixation, *Prog. Oceanogr.*, 77, 56–82,  
1399 2008.
- 1400
- 1401 Zalesak, S. T.: Fully multidimensional flux corrected transport algorithms for fluids, *J. Comput. Phys.*, 31, 335–362, 1979.
- 1402
- 1403 Zhang, J. and Rothrock, D.A.: Modeling global sea ice with a thickness and enthalpy distribution model in generalized  
1404 curvilinear coordinates, *Mon. Wea. Rev.* 131(5), 681-697, 2003
- 1405
- 1406 Zobler, L.: A World Soil File for Global Climate Modelling. NASA Technical Memorandum 87802. NASA Goddard  
1407 Institute for Space Studies, New York, New York, U.S.A., 1986.